International Journal of Heat and Mass Transfer 255 (2026) 127897

Contents lists available at ScienceDirect

International Journal of Heat and Mass Transfer

journal homepage: www.elsevier.com/locate/ijhmt

# Nature-inspired lotus-shaped fins combined with hybrid nanoparticles and metal foam for high-performance latent heat thermal energy storage

Prashant Saini [a,*], Julian D. Osorio [b,*], Munjal P. Shah [a], Umang N. Patel [a], Akhil Nelapudi [c], Luis A. Porto-Hernandez [d]

[a] Centre for Energy Conversion & Storage Systems, National Renewable Energy Laboratory (NREL), Golden, CO 80401, United States
[b] Building Technologies and Science Center, National Renewable Energy Laboratory (NREL), Golden, CO 80401, United States
[c] Mechanical Engineering Department, Clemson University, North Charleston, SC, 29404, United States
[d] Universidad Tecnológica de Bolívar, Escuela de Ingeniería, Arquitectura & Diseño, Cartagena de Indias 130010, Colombia

ARTICLE INFO

*Keywords:*
Nature-inspired shaped fins
Phase change material
Melting/charging
Solidification/discharging
Thermal energy storage
Performance enhancement

ABSTRACT

Latent heat thermal energy storage (LHTES) systems play a critical role in renewable energy integration by providing high energy density and nearly isothermal operation during phase transitions. However, their performance is often limited by slow melting/charging rates, which motivates the search for enhanced heat transfer designs. This study investigates the melting behavior of RT-82 phase change material (PCM) using novel lotus-shaped fins combined with copper metal foam and conductive graphene nanoparticles and carbon nanotubes. A two-dimensional enthalpy–porosity model in ANSYS Fluent was developed to simulate the charging/melting process, capturing non-thermal equilibrium between the foam and PCM/nano-PCM. In this study, effects of fin geometry, nanoparticle concentration, and foam porosity on melting dynamics and cost-performance trade-offs were investigated. Results showed that natural convection accelerated melting by ~12% compared to conduction-only scenarios. Optimized lotus-shaped fins with higher fin density (T3F4 and T3F10) achieved up to 63% faster melting relative to sparse configurations. Graphene nanoparticles improved thermal conductivity, with a 6% volume fraction, by reducing melting time by ~6.9%, while their combination with 75% porosity foam achieved a maximum reduction in the melting time of ~51% compared to pure PCM. Cost-performance analysis identified T3F4 as the most balanced design, offering rapid thermal response without excessive material costs, while moderate-density designs like T3S6 provided economical alternatives with acceptable performance. These results highlight the performance enhancement that can be achieved by integrating bio-inspired fins, nanoparticles, and foams, into compact and efficient LHTES for solar heating, building thermal management, and industrial waste-heat recovery applications.

## 1. Introduction

As global energy consumption continues to rise, there is a pressing need for innovative, effective, and resilient methods for storing energy. Thermal energy storage (TES) emerges as a promising technology among various methods for energy storage. Compared with electrical and electrochemical storage options, TES offers significant benefits, including extended operational lifespans, reduced technological costs, and higher storage density [1–3]. Generally, TES technologies are typically grouped into three primary categories: latent heat TES (LHTES) [4,5], chemical-TES (CTES) [6], and sensible heat-TES (SHTES) [7].

LHTES stands out as an efficient thermal storage technology/method because it can accumulate large amounts of energy within a compact volume and function at almost the constant temperatures during both charging and discharging, owing to the nearly isothermal characteristics of phase transitions. Additionally, LHTES provides notable chemical stability and operational safety, making it cost-effective and highly suitable for large-scale use in industrial processes and building energy systems [8–10]. Potential applications of LHTES have been increasingly highlighted in recent studies. For instance, in renewable energy systems, as a mean to store surplus solar thermal energy, particularly in concentrated solar power plants. In buildings, LHTES systems could provide heating and cooling flexibility, lowering peak electricity demand and improving energy efficiency. Industrial operations may benefit through the recovery and reuse of waste heat, thereby reducing

* Corresponding authors.
*E-mail addresses:* Prashant.Saini@nrel.gov (P. Saini), Julian.Osorio@nrel.gov (J.D. Osorio).

https://doi.org/10.1016/j.ijheatmasstransfer.2025.127897
Received 11 August 2025; Received in revised form 15 September 2025; Accepted 25 September 2025
Available online 3 October 2025

**Nomenclature**

| | |
|---|---|
| $A_{sf}$ | Surface area ($m^2$) |
| $A_m$ | Mushy zone numerical coefficient |
| $B$ | Boltzmann constant ($1.381 \times 10^{-23}$ J/K) |
| $C_f$ | Inertial coefficient of porous resistance |
| $C_{mush}$ | Mushy zone constant |
| $c_p$ | Specific heat capacity at constant pressure (J/kg·K) |
| $(c_p)_f$ | Specific heat capacity of nano-PCM (J/kg·K) |
| $(c_p)_{hnf}$ | Specific heat capacity of the hybrid nanoparticle (J/kg·K) |
| $(c_p)_{np}$ | Specific heat capacity of nanoparticles (J/kg·K) |
| $(c_p)_{PCM}$ | Specific heat capacity of PCM (J/kg·K) |
| $(c_p)_{s1}$ | Specific heat capacity of nanoparticle 1 (J/kg·K) |
| $(c_p)_{s2}$ | Specific heat capacity of nanoparticle 2 (J/kg·K) |
| $d_l$ | Ligament diameter (m) |
| $d_{np}$ | Diameter of nanoparticle (m) |
| $d_p$ | Pore diameter (m) |
| $e$ | Empirical structural correction factor |
| $f\,(T,\phi)$ | Function of Brownian motion |
| $\bar{f}_l$ | Mean liquid fraction |
| $h$ | Specific enthalpy (J/kg) |
| $h_{sf}$ | Interfacial heat transfer coefficient ($W/m^2$·K) |
| $K$ | Permeability of the foam ($m^2$) |
| $L$ | Latent heat of fusion (J/kg) |
| $(L)_f$ | Latent heat of nano-PCM (J/kg) |
| $L_{hnf}$ | Latent heat of hybrid nanoparticle (J/kg) |
| $p$ | Pressure (Pa) |
| $Pr$ | Prandtl number |
| $Re_d$ | Reynolds number |
| $S_e$ | Energy source term ($W/m^3$) |
| $sf$ | Shape factor |
| $S_u$ | Source term in x-momentum equation |
| $S_v$ | Source term in y-momentum equation |
| $t$ | Time (s) |
| $T$ | Temperature (K) |
| $T_0$ | Initial temperature (K) |
| $T_f$ | Temperature of liquid phase (K) |
| $T_{pl}$ | Liquidus temperature (K) |
| $T_{ps}$ | Solidus temperature (K) |
| $T_{ref}$ | Reference temperature (K) |
| $T_s$ | Temperature of solid phase (K) |
| $T_w$ | Wall temperature (K) |
| $u$ | Velocity in x-direction (m/s) |
| $v$ | Velocity in y-direction (m/s) |
| $w$ | Velocity in z-direction (m/s) |

*Greek symbols*

| | |
|---|---|
| $\beta_f$ | Thermal expansion coefficient of nano-PCM (1/K) |
| $\beta_{hnf}$ | Thermal expansion coefficient of hybrid nano-PCM |
| $\beta_k$ | Brownian motion enhancement factor |
| $\beta_{np}$ | Thermal expansion coefficient of nanoparticles (1/K) |
| $\beta_{PCM}$ | Thermal expansion coefficient of PCM (1/K) |
| $\Delta h$ | Latent heat component in energy source (J/kg) |
| $\varepsilon$ | Porosity of the metal foam |
| $\Gamma$ | Boundary surfaces |
| $\Gamma_{sh}$ | Shell boundary surface |
| $\Gamma_{tu}$ | Inner wall boundary |
| $\lambda$ | Thermal conductivity (W/m.K) |
| $\lambda_{bf}$ | Thermal conductivity of base fluid (W/m·K) |
| $\lambda_f$ | Thermal conductivity of nano-PCM (W/m·K) |
| $\lambda_{fe}$ | Effective thermal conductivity of fluid phase (W/m·K) |
| $\lambda_{hnf}$ | Thermal conductivity of hybrid nanoparticle (W/m·K) |
| $\lambda_{np}$ | Thermal conductivity of nanoparticles (W/m·K) |
| $\lambda_{PCM}$ | Thermal conductivity of PCM (W/m·K) |
| $\lambda_{s1}$ | Thermal conductivity of nanoparticle 1 (W/m·K) |
| $\lambda_{s2}$ | Thermal conductivity of nanoparticle 2 (W/m·K) |
| $\lambda_{se}$ | Effective thermal conductivity of solid matrix (foam) (W/m·K) |
| $\sigma$ | Standard deviation |
| $\phi$ | Nanoparticle volume fraction |
| $\phi_1$ | Volume fraction of nanoparticle 1 |
| $\phi_2$ | Volume fraction of nanoparticle 2 |
| $\xi$ | Numerical fitting parameter |
| $\nu$ | Thermal expansion coefficient (1/K) |

*Acronyms*

| | |
|---|---|
| AMG | Algebraic multigrid |
| CNT | Carbon nanotube |
| CTES | Chemical thermal energy storage |
| HTF | Heat transfer fluid |
| HVAC | Heating, ventilation, and air conditioning |
| LHTES | Latent heat thermal energy storage |
| PCM | Phase change material |
| PPI | Pores per inch |
| SHTES | Sensible heat thermal energy storage |
| TES | Thermal energy storage |
| TTHE | Triplex tube heat exchanger |

fuel consumption and emissions. Furthermore, their compactness and safety make them a promising alternative for coupling with district heating, thermal energy networks, and other large-scale energy systems.

LHTES systems utilizing phase change materials (PCMs) have garnered considerable attention because of their ability to store large amounts of energy while maintaining nearly uniform temperatures during phase transitions [11,12]. Despite their advantages, most PCMs have low thermal conductivity, which limits the overall heat transfer, reducing system performance. To address this drawback, scientists have examined different enhancement methods such as dispersing highly conductive nanoparticles, employing optimized fin geometries, and creating composites materials that integrate metal foams to boost thermal conductivity and efficiency [13,14]. Integrating innovative fins into LHTES systems is a widely adopted strategy, which significantly improves thermal performance [15]. Extensive research has been conducted in this area, focusing on design and optimization of various advanced fin configurations, including triangular fins [16], fractal fins [17,18], snowflake fins [19,20], reticular fins [21], tree-shaped fins [22, 23], and smoothed optimized flat-plate fins [24], among other innovative designs. These studies highlight the ongoing pursuit of enhanced thermal efficiency through novel fin geometries. Commercial LHTES units typically employ rectangular/annular straight fins; while manufacturable, their gains, mainly from added conduction area, are often modest. For example, radial fins can raise average melting rate by ~20%, and halving fin spacing can cut melting time by ~40% in shell-and-tube systems [18]. Moving beyond these baselines, tree-shaped/fractal fins improve temperature uniformity and accelerate phase change; a 3D vertical fins study reports 34.5% shorter melting and 49.2% shorter solidification, with time-averaged storage/release rates up by 49.4%/96.4% versus conventional finned units [23]. Consistent with this trend, optimized Y-shaped (branched) fins increased discharging efficiency by ~24% relative to a baseline design under matched PCM volume [18]. In parallel, snowflake-type internal geometries coupled with hybrid nano-PCM have shown additional material–geometry synergy; for example, an $Al_2O_3$–GO hybrid at a volumetric fraction of 0.04 achieved a 24.1% increase in solidification rate

compared with pure PCM in a snowflake LHTESS [20]. While these geometries mimic fractal or branching principles, systematic exploration of designs inspired by lotus morphology has been undertaken. The lotus leaf distributed surface patterns and hierarchical branching, offering a unique pathway for simultaneously enhancing radial and axial heat transport in LHTES, is a concept not yet examined in the literature. To clarify the origin of this bio-inspired concept, Fig. 1 illustrates the natural lotus flower. In nature, the lotus leaf and flower exhibit a radial vein–petal structure extending outward from a central core. This geometry ensures uniform transport of nutrients and mechanical stability across the surface. Translating this principle into fin design, the lotus-inspired arrangement provides multiple conduction pathways from the central tube to the PCM, reducing thermally inactive regions and promoting more uniform phase change. Thus, the lotus morphology offers a natural blueprint for achieving simultaneous radial and axial heat transport, which forms the foundation of the fin geometries explored in this study.

Pu et al. [25] observed that incorporating fins into LHTES systems significantly improved melting/charging efficiency, reducing the total melting/charging time by 44% in comparison to the systems lacking fins. Zhang et al. [26] found that a snowflake-shaped fin configuration accelerate the solidification/discharging process up to 35% compared to longitudinal fins, and a 50% improvement over systems without fins. Rozenfeld et al. [27] developed a helical fin structure used within a dual-tube setup, which effectively enhanced the PCM's melting/charging rate and supported more efficient system operation. Mao et al. [28] introduced a bifurcated fin design in an LHTES storage system, which showed a better melting/charging performance than traditional longitudinal fins. Further studies by Elmaazouzi et al. [29] and Nie et al. [30] emphasized that the thermal performance of such systems is strongly influenced by the number of fins and fin characteristics, including size and shape. Zonouzi and Dadvar [31] conducted a comparative analysis of helical and longitudinal fins, concluding that the use of helical fins led to an 18.25% reduction in total melting/charging time relative to longitudinal fins. Similarly, He et al. [32] observed that helical fins caused minimal disruption to natural convection during the solidification phase and facilitated enhanced multi-directional circulation within the annular space, thereby improving heat transfer efficiency. Zhang et al. [33] assessed a vertical tube and shell LHTES system incorporating distinct fin geometries for such as annular, longitudinal, and helical types and reported that the helical fin design decreased the melting/-charging duration by 9.9% and 31% when compared to annular and longitudinal fins, respectively. In their study, Zarei et al. [34] assessed the effect of different fin characteristics, including fin size, its arrangement, and the angle formed between the tube wall and the longitudinal copper fins, to observe the discharging/solidification rate of PCMs. They concluded that a mixed fin design led to a substantially improved discharging/solidification process, reducing the total solidification/discharging time by about 42% in comparison to systems lacking fins. In the context of LHTES systems heated from the sidewalls, Nakhchi et al. [35] introduced a stepped fin configuration, which exhibited much faster melting/charging behavior than flat horizontal fins, achieving a 65.5% higher melt rate within 3600 seconds. Yang et al. [36] addressed the challenge of uneven PCM melting/charging by implementing annular fins with a non-uniform spatial distribution. This approach notably improved thermal response, resulting in a 62.8% shorter melting/charging time and a 34.4% improvement in thermal uniformity. To further reduce charging times in fin-enhanced LHTES units, Wang et al. [37] proposed a finned-plate architecture and examined the effect of variations in fin designs on the melting/charging performance. They observed that advanced configurations such as rippled fins and fins of differing lengths, increasing fin thickness and length, significantly promoted paraffin melting/charging efficiency. Experiment performed by Baby and Balaji [38] assessed the performance of aluminum pin fins configuration in three quantities (33, 72, and 120 pin) and found the 72-pin setup provided the most efficient melting/charging, indicating optimal thermal interaction in PCM-pin fin systems.

A major drawback of these considered methods is the added volume and/or weight, which restricts their use in designing compact and lightweight thermal storage systems. Additionally, these techniques can hinder the natural convection-driven fluid motion of the PCM during phase transitions, thereby diminishing its positive impact on heat transfer. An alternative to address this challenge involves dispersing highly conductive nanoparticles into the PCMs, which increases the overall thermal conductivity while preserving a more fluid-like behavior during the phase change [39–41]. The incorporation of nanoparticles into PCMs to improve their thermophysical properties was explored numerically by Khodadadi and Hosseinizadeh [42], who demonstrated that such additives can significantly increase thermal conductivity, making them promising for TES systems. Mahdi et al. [43] extended this investigation to triplex tube heat exchangers, revealing that a nanoparticle concentration of just 0.05 volume fraction could reduce melting/charging time by as much as 90%. However, despite these improvements, fins have proven to be more effective than nanoparticles in accelerating the charging/melting process when occupying the same volume within the PCM, as highlighted by Mahdi et al. [44] through computational fluid dynamics analysis. One major limitation of nano-PCMs is their tendency to inhibit natural and forced convection, which can adversely affect melting/charging efficiency. This phenomenon was explored by Mohamad [45] through two-dimensional simulations, which showed that enhanced thermal conduction due to nanoparticles leads to a systematic temperature distribution within the liquid PCM. As a result, the reduced thermal gradient weakens the

(a) (b)

**Fig. 1.** (a) Lotus flower exhibiting radial petal arrangement in nature. (b) Lotus-inspired fin geometry derived from this morphology, which is designed to promote uniform heat distribution and accelerate phase change in LHTES systems.

buoyancy-driven convection flow, thereby lowering the heat transfer contribution from the natural convection. Researchers have extended this approach by developing hybrid nanofluids and hybrid nano-PCMs that combine two or more types of nanoparticles to achieve better thermal performance and stability than single-particle systems. Hosseinpour et al. [46] investigated single-walled carbon nanotube–CuO/$H_2O$ hybrid nanofluids in a helical-coil LHTES unit and reported 39.24% reduction in melting time. Hassan et al. [47] demonstrated that ZnO/$Fe_2O_3$ hybrid nano-PCMs dispersed in paraffin improved both melting/freezing efficiency and cycle stability. Similarly, Sadiq et al. [48] examined $Al_2O_3$/CuO hybrid nano-PCMs in triplex-tube configurations, showing charging-time reductions of up to 19%. Collectively, these studies highlight that hybrid formulations of nano-PMCs can mitigate some of the drawbacks of conventional nano-PCMs while providing enhanced heat transfer for TES applications.

In addition to using fins and nanoparticles for enhancing the rate of phase change, incorporating open-cell metal foams into PCMs has gained attention as a highly effective method to enhance thermal conductivity. Zhao and Tian [49] conducted experiments using paraffin RT58 integrated with copper foam, subjecting the system to a constant heat flux from the bottom. Their results demonstrated that incorporating copper foam markedly improved the melting/charging performance. In a separate experimental investigation, Chen et al. [50] explored the melting/charging characteristics of PCMs embedded in aluminum foam, utilizing both infrared imaging and optical microscopy to visualize melting/charging at the pore level. The study concludes a substantial enhancement in the melting/charging rate using high-porous metal foam. Li et al. [51] executed an experimental study to evaluate the thermal behavior of PCMs incorporated into copper foams with different porosities and pore dimensions. Their results demonstrated that the enhanced thermal conductivity due to the copper foam significantly accelerated the melting/charging process. Furthermore, they observed that foams with higher open porosity facilitated faster heat transfer due to increased PCM-copper contact area, while variations in pore dimensions influenced the balance between conduction pathways and fluid movement during phase change. Zhou and Zhao [52] investigated the transient charging/melting performance of paraffin integrated with copper metal foam and found that the presence of the copper foam increases the phase transition rate by two times in comparison to pure paraffin. Additionally, Yang et al. [53] analyzed the impact of enclosure orientation on melting/charging behavior, comparing systems with and without metal foam under tilt angles of 90°, 60°, 30°, and 0°. Their results revealed that inclination significantly influenced the melting/-charging performance of pure PCMs but had minimal effect when metal foam was used. In summary, the main primary mechanism behind heat transfer improvement using fins is increasing the effective convective surface area. Fins help transfer heat from the wall of the heat transfer fluid (HTF) channel to the inner regions of the PCM. While the PCM adjacent to the fins benefits from this conduction pathway, regions farther from the fins remain less thermally active because of the poor thermal conductivity of the PCM alone. To accelerate the phase change process, additional fins can be introduced; however, this comes with a cost of a reduction in the PCM volume, thereby lowering the system's energy storage capacity. A more space-efficient solution with enhanced thermal performance involves using open-cell metal foam impregnated with nano-PCM. This porous structure allows for a more uniform heat distribution within the storage medium. Integrating highly conductive fins with metal foam creates a synergistic effect, where heat is initially transferred from the HTF wall through the fins and then evenly spread throughout the nano-PCM via the interconnected ligaments of the metal foam.

In addition to these design-oriented approaches, recent advances in numerical modeling have significantly improved the understanding of phase change dynamics using the enthalpy–porosity method. Ye and Arici [54] redefined the computational treatment of local and global interface errors and validated a 2D gallium melting simulation against experimental data. In a subsequent study, they extended this framework to a 3D enthalpy–porosity modeling [55], strictly analyzing the feasibility of replacing 3D simulations with simplified 2D approaches and developing improved correlations for liquid fraction and mean liquid layer thickness. They further examined the relationship between the mushy zone constant and driving temperature difference [56], establishing correlations and validation results that aid parameter selection in phase change modeling. More recently, Ye and Arici [57] identified issues such as convective false diffusion and asymmetrical phase-change interfaces, linking them to equilibrium phase-change behavior through dimensionless correlations. Collectively, these studies highlight the strengths and limitations of enthalpy–porosity modeling and provide a solid theoretical foundation for applying this method to novel LHTES systems. The existing literature has made key contributions to improving LHTES performance. Advanced fin geometries have been shown to accelerate melting/charging by increasing heat transfer surfaces, though often at the cost of PCM volume. Nanoparticles enhance conductivity but may suppress natural convection at higher volume fractions. Metal foams provide effective conduction pathways and more uniform melting but reduce available PCM and energy density. Refined numerical models have validated enthalpy–porosity approaches and clarified the role of parameters such as the mushy zone constant. These contributions collectively highlight that while significant progress has been made in improving PCM melting/charging performance, a gap remains in integrating bio-inspired geometries with hybrid nanoparticles and foams in a single system, which is the focus of this study. Although previous studies have examined fractal and tree-like fins, nano-PCM composites, or metal-foam structures, these approaches have largely been considered separately or in limited pairwise combinations. The present work is distinct becuase it integrates a lotus-inspired fin geometry together with hybrid nanoparticles and copper foam in a single LHTES system. The lotus fin arrangement is designed to improve both radial and axial heat transport while maintaining PCM volume, which helps reduce thermally inactive regions. When combined with the high-conductivity network of the metal foam and the tailored conductivity of hybrid nanoparticles, the system achieves a coordinated enhancement that has not been reported in earlier studies. To the best of our knowledge, this is the first attempt to adapt lotus-inspired branching and surface-distribution patterns into LHTES fin design. Unlike fractal, tree-like, or snowflake geometries, which emphasize either symmetry or hierarchical spreading, the lotus morphology uniquely combines both features. Embedding this design within a hybrid nano-PCM/copper foam framework establishes a bio-inspired, multi-scale approach that goes beyond existing enhancement strategies.

In this work, nature-inspired fin designs are proposed and analyzed as they offer a promising pathway to improving the storage capacity and effectiveness of LHTES to enhance system thermal performance. These structures, mimicking efficient biological heat transfer structures, enhance conductive and convective mechanisms within the PCM matrix. Combining the lotus-shaped fin design, investigated in this study, maximizes heat transfer surface area and minimizes thermal resistance, leading to a more rapid PCM phase change process. While existing research has explored a range of fin geometries, including fractal and tree-like structures, further investigation is required to evaluate the most effective integration of bio-inspired fin designs with hybrid nanoparticles and metal foams. This study aims to bridge that gap by analyzing the thermal behavior of a LHTES system incorporating a lotus-inspired fin structure alongside hybrid nanomaterials and porous metal frameworks. The key objectives include: (i) evaluating the influence of the non-standard fin geometry on PCM melting/charging, (ii) optimizing the best structural geometry to enhance overall system performance, and (iii) assessing the effect of hybrid nanoparticles and metal foams on thermal conductivity. By integrating bio-inspired fin structures, hybrid nanoparticles, and metal foams, this study aims to advance the development of highly efficient LHTES systems suitable for multiple thermal energy conversion applications, industrial waste heat recovery,

and building thermal management. The conclusion will offer useful insights for future thermal energy storage solutions, fostering the integration of innovative design strategies into practical energy systems.

## 2. Model and solution approach

### 2.1. Model formulation and description

This study investigates the melting (charging) behavior and the corresponding thermal efficiency of a LHTES system using a horizontal shell-and-tube configuration. The analysis accounts for the impacts of natural convection within the PCM. Various design modifications are explored, including changes in fin geometries and the integration of metal foams and nanoparticles to enhance heat transfer performance. As illustrated in Fig. 2 (a), the system consists of a central tube through which the hot HTF flows, while the PCM is placed in the annular region between the outer and inner tubes. Previous investigations [58,59] have indicated that for cylindrical PCM enclosures with circumferentially uniform wall temperature, conduction in the solid PCM is predominantly radial, while the liquid PCM heat transfer is convection-dominated; axial variations exist but are weaker than radial ones over typical operating ranges. Therefore, a two-dimensional symmetric was sufficient to capture the dominant physics of the melting mechanism, as illustrated in Fig. 2 (b). Fins are commonly used in thermal systems to increase the effective heat exchange surface area, particularly in space-constrained applications. Moreover, they are easier to fabricate and offer quicker thermal response [60]. The geometric configuration for this analysis is based on the model presented by Kazemi et al. [61] with modifications shown in Fig. 2 (a). The analysis assumes negligible shell and tube wall thickness. The inner and outer diameters are set at 16 mm and 70 mm, respectively, defining an annular gap of 54 mm. The storage unit's length is considered to be 500 mm. Thermal insulation is assumed around the outer shell, mimicking real-world insulation practices to limit heat loss. The system is initially at 27 °C, below the PCM's melting point, while the HTF is supplied at 90 °C with a mass flow rate of 0.01 kg/s. This temperature corresponds to low-temperature TES applications such as district heating, building thermal management, and recovery of low-grade industrial waste heat. Based on recommendations from earlier studies [58,59] the fin volume fraction is fixed at 10% to achieve optimal heat storage performance. Fin length remains unchanged throughout, while thickness is adjusted to examine its effect on melting dynamics. The PCM used is RT-82, selected for its reliability in practical applications, and copper is chosen as the fin's material due to its excellent thermal conductivity and relatively low cost. The choice of RT-82 as PCM aligns with the operating range, where natural convection plays a dominant role in melting dynamics. Extending the framework to high-temperature systems (e.g., >400 °C for concentrated solar power or industrial processes) would require different PCM, and consideration of high-temperature material stability. The influence of nanoparticles, specifically graphite, carbon nanotube (CNT) and the hybrid nanoparticle (combination of both graphite and CNT), each with an average size of 29 nm is also explored to assess their potential in enhancing thermal performance. To minimize the computational effort, only half of the system's geometry is simulated, leveraging its symmetrical nature, as illustrated in Fig. 2 (c). The study proposes 15 distinct fin configurations aimed at improving melting and charging efficiency, and these are also compared against systems enhanced with metal foam and nanoparticles. These 15 distinct fin layouts are illustrated in Fig. 2 (d). In these designs, T denotes the geometry type, NF refers to the no-fin configuration, S indicates a symmetric fin arrangement, A represents an asymmetric fin arrangement, and the number represents the number of fins in the particular configuration. This study employed cubic spline interpolation (i.e., Bezier curve) to design fins, generating continuous and smooth geometric profiles from design points defined by their spatial coordinates. Each design configuration, i.e., Type-1, Type-2, and Type-3 consists of four data points, denoted as p1 to p4, with corresponding x and y values representing the horizontal and vertical coordinates, respectively. These points serve as interpolation nodes for constructing a piecewise cubic function across three segments.

$$y(x) = a_i(x - x_i)^3 + b_i(x - x_i)^2 + c_i(x - x_i) + d_i$$

The coefficients $a_i$, $b_i$, $c_i$ and $d_i$ are determined such that the curve is $C^2$ continuous, ensuring a smooth and physically realistic shape. For instance, in Type-1, the four points are interpolated sequentially, with continuity conditions ensuring $C^2$ smoothness across segments. Due to non-monotonicity in the x-values, the interpolation is implemented in parametric form x(t), y(t), where $t \in [0,1]$ represents a normalized parameter space, enabling accurate modeling of arbitrary spatial curves. Point t1 in Table 1 represents the location of the tip of the additional center-fin, as shown in designs (I) – (III) in Fig. 2 (e). Table 1 lists the X and Y coordinates (in mm) of key design points used to define the shape of an additional center-fin in three configurations: Type-1, Type-2, and Type-3. These points represent the outline of the fin's shape and are used to generate a smooth curve using cubic spline interpolation. For each fin type, four control points (labeled p1 to p4) are defined, which determine the shape of the fin from base to near its tip. An extra point, labeled t1, marks the tip of the center-fin. These coordinates are used as input to create a smooth fin profile in a 2D plane. Table 2 compiles the thermophysical characteristics of all materials utilized in the simulation. Table 3 represents the 15 different geometric configurations with fins on the inner and outer cylinders of the LHTES system with their identifiers. Table 4 illustrates further study performed for the different scenarios with the best geometry configuration (i.e., T3F10) among the 15 geometric configurations as represented in Table 3. Each simulation in Table 4 is labeled with a unique identifier that encodes the type and composition of the PCM. The identifier follows a structured format to represent the presence of nanoparticle additives and metal foam. Specifically, the letters "C" and "G" denote CNT and graphene nanoparticles, respectively, while the number following these letters indicates the volume fraction of the corresponding nanoparticle. The letter "M" followed by a number (e.g., M75, M95) signifies the inclusion of metal foam with the specified pore density in PPI. Composite identifiers such as "C4M85" or "G2M98" indicate hybrid configurations that combine CNT or graphene with metal foam, where, for example, "C4M85" corresponds to 4% CNT and 85 PPI metal foam. Cases labeled as "M75", "M85", etc., contain only metal foam without nanoparticles. Identifiers starting with "H" (e.g., H1, H5) represent hybrid nano-enhanced PCM cases containing both CNT and graphene in varying proportions without metal foam. This naming convention provides a concise and systematic way to distinguish between the various PCM enhancement strategies considered in the study.

### 2.2. Numerical approach

The present work employs ANSYS Fluent 25 R1 to conduct numerical simulations. Heat transfer and phase change phenomena within the LHTES system are examined using a finite volume-based approach. To handle the coupling between pressure and velocity fields, the SIMPLE algorithm is adopted for numerical stability and convergence. For spatial discretization, a second-order upwind scheme was implemented to achieve higher numerical accuracy. The pressure field was corrected through the PRESTO! interpolation approach. To improve computational performance and ensure faster convergence, the algebraic multigrid (AMG) method was applied. The simulation employed underrelaxation factors of 0.7 for momentum, 0.3 for pressure, and 1.0 for both density and energy equations, which are consistent with the recommended values in the ANSYS Fluent user's guide for buoyancy-driven convective flows, ensuring numerical stability and convergence [62]. Convergence criteria were satisfied once all residuals dropped below $10^{-8}$.

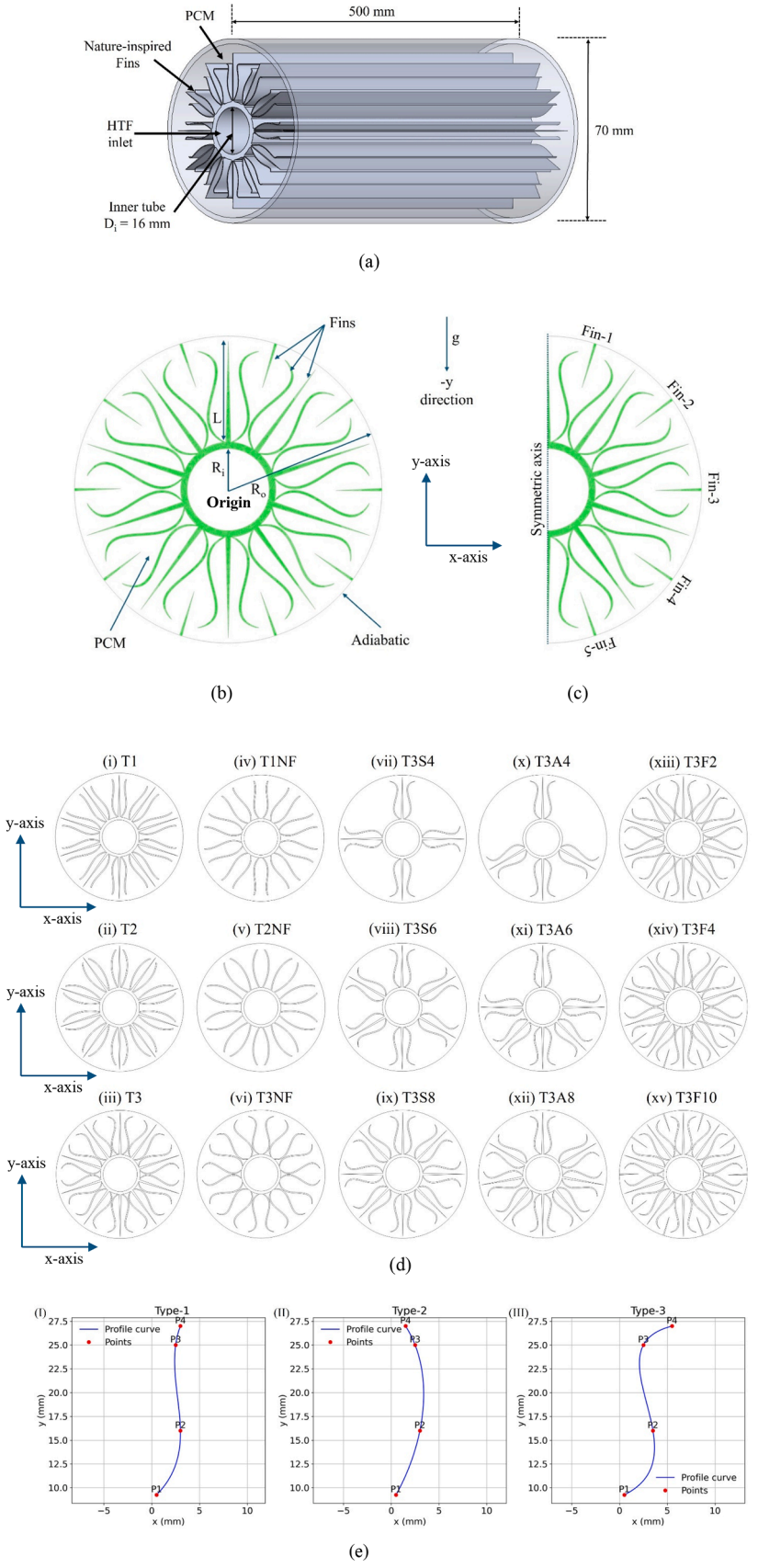


**Fig. 2.** Design illustration of a nature-inspired-finned LHTES system (a) 3D illustration of a horizontal-axis shell-and-tube LHTESS with nature-inspired fins, (b) Two-dimensional finned LHTES system, (c) Two-dimensional symmetrical domain of the finned LHTES system, (d) 15 distinct fin configurations used in the current study, and (e) Bezier curves for Type-1 (T1), Type-2 (T2) and Type-3 (T3) fin designs.

**Table 1**
Spatial coordinates (in mm) of control points and tip for additional center fin designs.

| | Type-1 | | Type-2 | | Type-3 | |
|---|---|---|---|---|---|---|
| Point | X | Y | X | Y | X | Y |
| p1 | 0.5 | 9.25 | 0.5 | 9.25 | 0.5 | 9.25 |
| p2 | 3 | 16 | 3 | 16 | 3.5 | 16 |
| p3 | 2.5 | 25 | 2.5 | 25 | 2.5 | 25 |
| p4 | 1.5 | 27 | 3 | 27 | 5.5 | 27 |
| t1 | 0 | 29 | 0 | 29 | 0 | 29 |

### 2.3. Governing equations used in the numerical model

To facilitate the mathematical modeling of the PCM charging/melting and melting/charging behavior within the LHTES system, the analysis is based on the assumptions as mentioned below: In the present model, several assumptions are applied to simplify the numerical formulation. The PCM is considered to exist as solid, liquid, and mixed solid - liquid during phase transition. All thermophysical properties of PCM/nano-PCM, except density, are assumed constant; this assumption is reasonable because paraffin-based PCMs exhibit only very small property variations in the studied range of 27 – 90 °C and the liquid PCM is treated as incompressible to simplify the continuity equation. Density variations due to temperature are incorporated using the Boussinesq approximation. Nanoparticles are uniformly dispersed within the PCM and are assumed to be in thermal equilibrium with the base PCM, with no relative motion between the two phases. A thermal non-equilibrium approach is adopted between the metallic foam ligaments and PCM/nano-PCM, allowing them to have distinct temperatures (i.e., $T_f \neq T_s$). The metallic foam is modeled as a homogeneous, isotropic, open-cell porous structure fully saturated with PCM. Natural convection within the PCM during melting is considered laminar, while viscous dissipation and volume shrinkage due to phase transition are neglected. The movement of individual PCM solid chunks in the liquid phase is disregarded. Finally, no external heat sources or losses are included, and system boundaries are treated as adiabatic.

Two stages of modeling were performed in this work. In the first stage, PCM melting without any enhancement structure was studied by solving the full conservation equations in Cartesian coordinates (Eqs. (1–4)). In the second stage, metal foam was embedded in the PCM to accelerate the melting process. For this case, the porous medium is represented using the volume-averaged formulation (Eqs. (23–27)) following Saini et al. [16]. Thus, the governing equations are presented in two sets corresponding to the two physical situations.

The transient heat transfer associated with the melting/charging process for pure PCM in the LHTES system is governed by the following equations:

The continuity equation is given in Eq. (1):

$$\frac{\partial u}{\partial x}+\frac{\partial v}{\partial y}=0 \tag{1}$$

The momentum equation is formulated as shown in Eq. (2):

$$\frac{\partial(\rho u)}{\partial t}+\mathrm{u}\frac{\partial(\rho u)}{\partial x}+v\frac{\partial(\rho u)}{\partial y}=-\frac{\partial p}{\partial x}+\frac{\partial}{\partial x}\left(\mu\frac{\partial u}{\partial x}\right)+\frac{\partial}{\partial y}\left(\mu\frac{\partial u}{\partial y}\right)+S_u \tag{2}$$

$$\frac{\partial(\rho v)}{\partial t}+\mathrm{u}\frac{\partial(\rho v)}{\partial x}+v\frac{\partial(\rho v)}{\partial y}=-\frac{\partial p}{\partial y}+\frac{\partial}{\partial x}\left(\mu\frac{\partial v}{\partial x}\right)+\frac{\partial}{\partial y}\left(\mu\frac{\partial v}{\partial y}\right)+S_v$$

The energy equation is defined by Eq. (3) for the fins and (4) for the PCM as follows:

$$\rho c_p(T)\frac{\partial T}{\partial t}=\frac{\partial}{\partial x}\left(\lambda\frac{\partial T}{\partial x}\right)+\frac{\partial}{\partial y}\left(\lambda\frac{\partial T}{\partial y}\right) \tag{3}$$

$$\frac{\partial(\rho h)}{\partial t}+\frac{\partial(\rho hu)}{\partial x}+\frac{\partial(\rho hv)}{\partial y}=\frac{\partial}{\partial x}\left(\lambda\frac{\partial T}{\partial x}\right)+\frac{\partial}{\partial y}\left(\lambda\frac{\partial T}{\partial y}\right)+S_e \tag{4}$$

In Eqs. (1) through (4), $\mu$ denotes the dynamic viscosity, $t$ is the time variable, $\rho$ stands for fluid density, $T$ refers to temperature, $u$ & $v$ represent the velocity components in the $x$ and $y$ directions, $x$ and $y$ represent the spatial coordinates in the horizontal and vertical directions. The term $h$ represents the total enthalpy, $\lambda$ indicates thermal conductivity, and $p$ corresponds to pressure. The source terms $S_e$, $S_u$, and $S_v$ enter the energy and momentum equations and are given by Eqs. (5), (6), and (7) as outlined in reference [16].

$$S_u=-uC_{mush}.\frac{(1-\beta)^2}{\beta^3+\xi} \tag{5}$$

$$S_v=-vC_{mush}.\frac{(1-\beta)^2}{\beta^3+\xi}+\rho\beta_T g(h-h_{ref}) \tag{6}$$

$$S_e=\rho L\frac{\partial\beta}{\partial t} \tag{7}$$

**Table 3**
Different geometric configurations with fins on the inner and outer cylinders of the LHTES system studied in the current analysis (see Fig. 2 (d)).

| Cases | Identifier | Geometry | # Fins on Inner wall | Inner central fin | Inner Fins-pattern | # Fins on outer wall |
|---|---|---|---|---|---|---|
| 1 | T1 | type-1 | 10 | Yes | Symmetric | - |
| 2 | T2 | type-2 | 10 | Yes | Symmetric | - |
| 3 | T3 | type-3 | 10 | Yes | Symmetric | - |
| 4 | T1NF | type-1 | 10 | No | Symmetric | - |
| 5 | T2NF | type-2 | 10 | No | Symmetric | - |
| 6 | T3NF | type-3 | 10 | No | Symmetric | - |
| 7 | T3S4 | type-3 | 4 | Yes | Symmetric | - |
| 8 | T3S6 | type-3 | 6 | Yes | Symmetric | - |
| 9 | T3S8 | type-3 | 8 | Yes | Symmetric | - |
| 10 | T3A4 | type-3 | 4 | Yes | Asymmetric | - |
| 11 | T3A6 | type-3 | 6 | Yes | Asymmetric | - |
| 12 | T3A8 | type-3 | 8 | Yes | Asymmetric | - |
| 13 | T3F2 | type-3 | 10 | Yes | Symmetric | 2 |
| 14 | T3F4 | type-3 | 10 | Yes | Symmetric | 4 |
| 15 | T3F10 | type-3 | 10 | Yes | Symmetric | 10 |

NF - No fin, S - Symmetric, A - Asymmetric

**Table 2**
Thermophysical characteristics of the various materials utilized in the study [16].

| S. No. | Thermophysical Property | RT-82 (PCM) | Copper | HTF | CNT | Graphene |
|---|---|---|---|---|---|---|
| 1. | Fusion Enthalpy (J/kg) | 176,000 | - | - | - | - |
| 2. | Phase Change Temperature Range (K) | 350.15/358.16 | - | - | - | - |
| 3. | Specific Heat (J/kg·K) | 2000 | 381 | 1745 | 9124 | 770 |
| 4. | Density (Solid / Liquid) (kg/m$^3$) | 950 / 770 | 8978 | 864.05 | 2100 | 2200 |
| 5. | Operating Temperature Reference Point (K) | 355.15 | - | 373.15 | - | - |
| 6. | Dynamic Viscosity (kg/m·s) | 0.03499 | - | 0.00299 | - | - |
| 7. | Thermal Conductivity (W/m·K) | 0.200 | 387.6 | 0.1200 | 3007.40 | 5000 |
| 8. | Thermal Expansion Coefficient (1/K) | 0.001 | - | - | 0.00002 | -0.000005 |

**Table 4**
Study performed for the different scenarios with the best geometry configuration (i.e., T3F10) (see Fig. 2 (d)).

| Case | Identifier | CNT (%) | Graphene (%) | Metal Foam (PPI) (%) | Case | Identifier | CNT (%) | Graphene (%) | Metal Foam (PPI) (%) |
|---|---|---|---|---|---|---|---|---|---|
| 16 | C2 | 2 | 0 | 0 | 38 | G2M75 | 0 | 2 | 75 |
| 17 | C4 | 4 | 0 | 0 | 39 | G4M75 | 0 | 4 | 75 |
| 18 | C6 | 6 | 0 | 0 | 40 | G6M75 | 0 | 6 | 75 |
| 19 | G2 | 0 | 2 | 0 | 41 | G2M85 | 0 | 2 | 85 |
| 20 | G6 | 0 | 4 | 0 | 42 | G4M85 | 0 | 4 | 85 |
| 21 | G6 | 0 | 6 | 0 | 43 | G6M85 | 0 | 6 | 85 |
| 22 | M75 | 0 | 0 | 75 | 44 | G2M95 | 0 | 2 | 95 |
| 23 | M85 | 0 | 0 | 85 | 45 | G4M95 | 0 | 4 | 95 |
| 24 | M95 | 0 | 0 | 95 | 46 | G6M95 | 0 | 6 | 95 |
| 25 | M98 | 0 | 0 | 98 | 47 | G2M98 | 0 | 2 | 98 |
| 26 | C2M75 | 2 | 0 | 75 | 48 | G4M98 | 0 | 4 | 98 |
| 27 | C4M75 | 4 | 0 | 75 | 49 | G6M98 | 0 | 6 | 98 |
| 28 | C6M75 | 6 | 0 | 75 | 50 | H1 | 0.5 | 1.5 | 0 |
| 29 | C2M85 | 2 | 0 | 85 | 51 | H2 | 1 | 1 | 0 |
| 30 | C4M85 | 4 | 0 | 85 | 52 | H3 | 1.5 | 0.5 | 0 |
| 31 | C6M85 | 6 | 0 | 85 | 53 | H4 | 1 | 3 | 0 |
| 32 | C2M95 | 2 | 0 | 95 | 54 | H5 | 2 | 2 | 0 |
| 33 | C4M95 | 4 | 0 | 95 | 55 | H6 | 3 | 1 | 0 |
| 34 | C6M95 | 6 | 0 | 95 | 56 | H7 | 1.5 | 4.5 | 0 |
| 35 | C2M98 | 2 | 0 | 98 | 57 | H8 | 3 | 3 | 0 |
| 36 | C4M98 | 4 | 0 | 98 | 58 | H9 | 4.5 | 1.5 | 0 |
| 37 | C6M98 | 6 | 0 | 98 | | | | | |

C - CNT, M - Metal foam, G - Graphene, H - Hybrid

The mushy zone coefficient $C_{mush}$ appearing in Eqs. (6) and (7) is set to a value of $10^7$ [16]. The variable $\beta$ indicates the liquid fraction of the PCM, $\xi$ indicates the correction factor, and $g$ denotes the gravitational acceleration. The specific heat is represented by $c_p$, while $\beta_T$ stands for the thermal expansion coefficient. The latent heat of fusion is $L$, $\Delta h$ refers to the latent heat contribution in the energy source term. The term $T_{ref}$ illustrates the defined reference condition, which in this work is taken as 30 °C. This value corresponds to typical ambient temperature used to mimic real-world conditions when initiating the charging/melting of the PCM.

Two complementary formulations are employed depending on the physical domain. Eqs. (1) – (4) describe the classical conservation equations (continuity, momentum with Boussinesq buoyancy and mushy damping, and energy) in Cartesian coordinates for pure PCM (no metal foam). When porous metal foam is present, additional hydrodynamic resistance and distinct thermal interactions between the PCM and the solid matrix arise. To represent these effects, the governing equations are recast in a porous-medium framework (Eqs. (23) – (27)), which include Darcy–Forchheimer drag in momentum and separate energy balances for the solid matrix and the PCM under local thermal non-equilibrium. The two sets of equations therefore address different physical cases and are not redundant.

To simulate the melting or charging phase in the LHTES system, the enthalpy-porosity approach is applied. Within this framework, the evolution of the liquid fraction is computed using Eq. (8), as detailed in reference [16].

$$\beta = \begin{cases} 0 \ (T \le T_{ps}) \\ \dfrac{T - T_{ps}}{T_{pl} - T_{ps}} \ (T_{ps} < T < T_{pl}) \\ 1 \ (T \ge T_{pl}) \end{cases} \tag{8}$$

$\beta$ takes a value of 1 when the PCM is fully liquid and 0 when it is completely solid. The temperatures $T_{ps}$ and $T_{pl}$ correspond to the solidus and liquidus temperature of the PCM, respectively. Within the mushy region, where the material is undergoing phase transition, $\beta$ varies continuously between 0 and 1. The total enthalpy or the total heat of the PCM, which includes both sensible and latent heat contributions, is determined using its liquid fraction and latent heat, Eq. (9) [16].

$$T(x, y, 0) = T_0$$
$$T|_{\Gamma_{tu}} = T_\omega \tag{9}$$
$$-\lambda \frac{\partial T}{\partial n}\bigg|_{\Gamma_{sh}} = 0$$

where $T_0$ is the initial PCM temperature, the variable $T_w$ represents the temperature of the inner tube wall, which is maintained at a temperature of 90 °C. The surfaces of the shell and inner wall are represented by $\Gamma_{sh}$ and $\Gamma_{tu}$, respectively. $\frac{\partial T}{\partial n}$ represents the change in temperature of PCM in the normal direction.

The thermophysical characteristics of nano-enhanced PCM are evaluated through a series of empirical correlations as mentioned in Eqs. (10) to (15).

The effective density of the nano-PCM is determined using Eq. (10) [16].

$$\rho_f = (1 - \phi)\rho_{PCM} + \phi\rho_{np} \tag{10}$$

The specific heat capacity is estimated as follows using Eq. (11) [16]:

$$(\rho c_p)_f = (1 - \phi)(\rho c_p)_{PCM} + \phi(\rho c_p)_{np} \tag{11}$$

The corresponding latent heat is calculated using Eq. (12) [16]:

$$(\rho L)_f = (\rho L)_{PCM}(1 - \phi) \tag{12}$$

The dynamic viscosity of the PCM infused with nanoparticle or nano-PCM is assessed via Eq. (13) [16].

$$\mu_f = \mu_{PCM} 0.983 e^{(12.959\phi)} \tag{13}$$

while Eq. (14) provides the formulation for the thermal expansion coefficient [16].

$$(\beta\rho)_f = (\beta\rho)_{np}\phi + (\beta\rho)_{pcm}(1 - \phi) \tag{14}$$

The effective thermal conductivity of nano-PCM is determined using Eq. (15) [16].

$$\lambda_f = \frac{\lambda_{np} - 2(\lambda_{PCM} - \lambda_{np})\phi + 2\lambda_{PCM}}{2\lambda_{PCM} + \lambda_{np} + (\lambda_{PCM} - \lambda_{np})\phi}\lambda_{PCM} + 5 \times 10^4 \beta_k \xi \rho_{PCM} \phi c_{p,PCM} \sqrt{\frac{BT}{d_{np}\rho_{np}}} f(T,\phi) \quad (15)$$

In Eq. (15), the first term represents the classical Maxwell-type contribution for nanoparticle suspensions, while the second term accounts for thermal enhancement due to Brownian motion of nanoparticles. To incorporate the influence of both temperature and nanoparticle concentration, the function *f (T, φ)* is employed, Eq. (16), based on the relation given in Ref. [16].

$$f(T,\ \phi) = \frac{(\phi \times\ 2.8217\ \times 10^{-2} + 3.917\ \times 10^{-3})}{T_l + (-3.0669\ \times 10^{-2}\phi - 3.91123\ \times 10^{-3})} \quad (16)$$

The factor $\beta_k$, which contributes to the Brownian motion enhancement factor, is calculated using an additional relation from Ref. [16].

$$\beta_k = 8.4407(100\phi)^{-1.07304} \quad (17)$$

Eqs. (10) through (17) utilize the following notations: $T$ represents the temperature, $d_{np}$ denotes the diameter of the nanoparticle, $B$ (i.e., the Boltzmann constant) has a value of $1.381 \times 10^{-23}$ J/K and the empirical constant $\xi$ accounts for particle–fluid interactions. $\phi$ represents the volume fraction of the nanoparticles. $(C_p)_f$ represents the specific heat capacity of nano-PCM, while $(L)_f$, $(\mu)_f$, $(\mu)_{PCM}$ are used to indicate latent heat capacity of nano-PCM, dynamic viscosity of nano-PCM and PCM. The symbol $(\beta)_f$, $(\beta)_{PCM}$, $(\beta)_{np}$ corresponds to the thermal expansion coefficient of nano-PCM, PCM and nanoparticles, and $(\rho)_f$, $(\rho)_{PCM}$, $(\rho)_{np}$ signifies the densities of nano-PCM, PCM and nanoparticles. $\lambda_f$, $\lambda_{PCM}$, & $\lambda_{np}$ represent the thermal conductivity of nano-PCM, PCM and nanoparticles.

Table 2 presents the thermophysical characteristics properties of the base PCM (i.e., RT-82) along with the hybrid nanoparticles (i.e., graphite and CNT). Key properties such as thermal conductivity, latent heat of fusion, density, and specific heat capacity of the hybrid nano-enhanced PCM are estimated utilizing a simplified theoretical mixing model, as described in Refs. [63,64].

$$\rho_{hnf} = \phi_2\rho_{s2} + \left[(1-\phi_1) + \phi_1\left(\frac{\rho_{s1}}{\rho_f}\right)\right](1-\phi_2)\rho_f \quad (18)$$

$$(\rho c_p)_{hnf} = \phi_2(\rho c_p)_{s2} + (\rho c_p)_f(1-\phi_2)\left[(1-\phi_1) + \phi_1\frac{(\rho c_p)_{s1}}{(\rho c_p)_f}\right] \quad (19)$$

$$(\rho L_f)_{hnf} = (1-\phi_1)(1-\phi_2)(\rho L_f)_f \quad (20)$$

$$\frac{\lambda_{hnf}}{\lambda_{bf}} = \frac{(sf-1)\lambda_{bf} + \lambda_{s2} - \phi_2(\lambda_{bf} - \lambda_{s2})(sf-1)}{\lambda_{s1} + \lambda_{bf}(sf-1) + \phi_2(\lambda_{bf} - \lambda_{s2})} \quad (21)$$

$$\lambda_{bf} = \lambda_f\frac{\lambda_{s1} + \lambda_f(sf-1) - \phi_1(\lambda_f - \lambda_{s1})(sf-1)}{\lambda_{s1} + \lambda_f(sf-1) + \phi_1(\lambda_f - \lambda_{s1})(sf-1)} \quad (22)$$

In Eqs. (18)-(22), $(c_p)_{hnf}$, $(c_p)_{s1}$, $(c_p)_{s2}$, and $(c_p)_f$, corresponds to the specific heat capacity of hybrid nanofluid, nanoparticles s1 & s2, and base fluid, $(\rho)_{hnf}$, $(\rho)_{s1}$, $(\rho)_{s2}$, and $(\rho)_f$ stands for densities of hybrid nanofluid, nanoparticles 1 & 2, and base fluid, and $(L)_{hnf}$, $(L)_f$ represents latent heat of hybrid nano-PCM and pure PCM. $\lambda_{hnf}$, $\lambda_{bf}$, $\lambda_{s1}$, and $\lambda_{s2}$ represent the thermal conductivity of hybrid nanofluid, base fluid, and nanoparticles 1 & 2. $\phi_1$ and $\phi_2$ represents the volume fraction of the nanoparticles 1 & 2. $sf$ is the shape factor.

This study employs a thermal conductivity model that captures the influence of nanoparticle-induced Brownian motion, incorporating factors such as particle diameter, concentration, and temperature. A correction factor, represented by ζ, is derived to reflect the thermal contribution from Brownian motion. Since such motion is limited to the liquid state of the PCM, ζ is applied exclusively within the liquid phase. To improve thermal performance, copper-based metal foam with a pore density of 40 PPI (pores per inch) is used.

The governing equations for the fluid flow and heat transfer within the PCM along with the porous medium are formulated in line with the framework provided by Saini et al. [16,44]. In the porous region containing metal foam, momentum transport is modeled using the Brinkman–Forchheimer extension of Darcy's law with a mushy-zone damping term to capture phase change effects. The superficial velocity vector is defined as $\vec{u} = (u,v)$, where $u$ and $v$ are the x- and y-components of the volume-averaged velocity, respectively, and are scalar fields. The magnitude of the velocity vector is defined as $|\vec{u}| = \sqrt{u^2+v^2}$. The $x$- and $y$-momentum balances are given in Eqs. (23) and (24). Thermal transport is treated under local thermal non-equilibrium, with separate solid and fluid energy equations coupled by an interfacial heat transfer coefficient $h_{sf}$ and specific area $A_{sf}$, as shown in Eqs. (25) and (26). The effective conductivities $\lambda_{se}$ and $\lambda_{fe}$ are defined in Eqs. (33) and (34). Mass conservation for incompressible flow with constant porosity is given by Eq. (27).

The conservation of momentum in the vertical *(y)* and horizontal *(x)* directions are formulated using Eqs. (23) and (24) as outlined in the references [16,44].

$$\rho_f\left(\frac{\partial v}{\partial t} + u\frac{\partial v}{\partial x} + v\frac{\partial v}{\partial y}\right) = -\frac{\partial p}{\partial y} + \mu_{eff}\left(\frac{\partial^2 v}{\partial x^2} + \frac{\partial^2 v}{\partial y^2}\right) - \frac{\mu_f}{K}v - \frac{C_F\rho_f}{\sqrt{K}}|\vec{u}|v - C_{mush}\frac{(1-\beta)^2}{\beta^3+\xi}v + \rho_f\beta_T g(T_f - T_{ref}) \quad (23)$$

$$\rho_f\left(\frac{\partial u}{\partial t} + u\frac{\partial u}{\partial x} + v\frac{\partial u}{\partial y}\right) = -\frac{\partial p}{\partial x} + \mu_{eff}\left(\frac{\partial^2 u}{\partial x^2} + \frac{\partial^2 u}{\partial y^2}\right) - \frac{\mu_f}{K}u - \frac{C_F\rho_f}{\sqrt{K}}|\vec{u}|u - C_{mush}\frac{(1-\beta)^2}{\beta^3+\xi}u \quad (24)$$

where $|\vec{u}| = \sqrt{u^2+v^2}$

To represent the thermal characteristics of the system under local thermal non-equilibrium conditions, the energy balance is modeled using Eqs. (25) and (26), following the methodology described in reference [16].

$$(1-\varepsilon)(\rho c_p)_s\left(\frac{\partial T_s}{\partial t}\right) = \nabla\cdot(\lambda_{se}\nabla T_s) + A_{sf}h_{sf}(T_f - T_s) \quad (25)$$

$$\varepsilon\rho_f c_{p,f}\left(u\frac{\partial T_f}{\partial x} + v\frac{\partial T_f}{\partial y} + \frac{\partial T_f}{\partial t}\right) = \nabla\cdot(\lambda_{fe}\nabla T_f) + h_{sf}A_{sf}(T_s - T_f) + \varepsilon\rho_f L\frac{\partial \beta}{\partial t} \quad (26)$$

The continuity equation for the porous domain of the metal foam is defined by Eq. (27):

$$\frac{\partial u}{\partial x} + \frac{\partial v}{\partial y} = 0 \quad (27)$$

In Eqs. (23) – (27), $T$ represents the temperature, $C_F$ denotes the inertial coefficient related to flow resistance in the porous medium, $L$ is the latent heat associated with the phase transition of the PCM, the effective thermal conductivity of the solid and fluid phases within the foam is denoted by $\lambda_{se}$ and $\lambda_{fe}$, the symbol $h_{sf}$ denotes the interfacial heat transfer coefficient between the PCM and the metal foam structure and $\mu$ is used for dynamic viscosity. The superficial velocity vector is defined as as $\vec{u} = (u,v)$, where $u$ and $v$ are the x- and y-components, respectively. Subscripts $s$ and $f$ refer to the solid matrix (i.e., metal foam) and the PCM (in both solid and liquid states). The porosity of the foam is given by $\varepsilon$, while $A_m$ is a numerical coefficient used for modeling the mushy zone during phase change, with a value of $10^7$ used in this study. In Eqs. (23) and (24), λ does not appear as these are momentum equations; only $\mu$ (dynamic viscosity), $K$ (permeability), and $C_F$ (inertial coefficient) are relevant. In Eqs. (25) and (26), $\lambda_{se}$ and $\lambda_{fe}$ denote the

effective thermal conductivities of the solid and fluid phases of the porous medium, respectively. These terms are defined in Eqs. (33) and (34).

The liquid fraction, denoted by $\beta_{PCM}$, is calculated using Eq. (28), as outlined in [16].

$$\beta_{PCM} = \begin{cases} 0 & T \le T_s \\ \dfrac{T - T_s}{T_l - T_s} & T_s < T < T_l \\ 1 & T \ge T_l \end{cases} \tag{28}$$

The structural configuration of the metallic foam, characterized by features such as overall porosity, ligament diameter and the pore density, plays a key role in influencing both thermal conductivity and fluid flow behavior. These parameters are illustrated below [16]:

$$\frac{d_l}{d_p} = 1.18\sqrt{\frac{1-\varepsilon}{3\pi}}\left(\frac{1}{1 - e^{-\frac{(1-\varepsilon)}{0.04}}}\right) \tag{29}$$

where

$$d_p = \frac{0.0254}{\omega} \tag{30}$$

Other important parameters, including inertial coefficient $(C_F)$ and permeability $(K)$, are estimated using empirical models proposed by Calmidi and Mahajan [65].

$$\frac{K}{d_p^2} = 0.00073(1-\varepsilon)^{-0.224\left(\frac{dl}{dp}\right)^{-1.11}} \tag{31}$$

$$C_F = 0.00212(1-\varepsilon)^{-0.132\left(\frac{dl}{dp}\right)^{-1.63}} \tag{32}$$

The effective thermal conductivity of the copper foam is evaluated using expressions provided in Eqs. (33) and (34) based on the approach described in [16].

$$\lambda_{se} = \left.\frac{\sqrt{2}}{2(M_B + M_A + M_D + M_C)}\right|_{\lambda_{f=0}} \tag{33}$$

$$\lambda_{fe} = \left.\frac{\sqrt{2}}{2(M_B + M_A + M_D + M_C)}\right|_{\lambda_{s=0}} \tag{34}$$

$$M_A = \frac{4\sigma}{\lambda_f(-2e^2 + 4 - \sigma\pi(-e+1))}$$

$$M_B = \frac{(-2\sigma + e)^2}{\lambda_s(-2\sigma + e)e^2 + (-4\sigma + 2e - (-2\sigma + e)e^2)\lambda_f}$$

$$M_C = \frac{\left(-2e + \sqrt{2}\right)^2}{\sigma^2 2\pi\left(-2e\sqrt{2} + 1\right)\lambda_s + 2\left(-2e + \sqrt{2} - \sigma^2\pi\left(-2e\sqrt{2} + 1\right)\right)\lambda_f}$$

$$M_D = \frac{2e}{\lambda_s e^2 + (-e^2 + 4)\lambda_f}$$

$$\sigma = \sqrt{\frac{\sqrt{2}\left(2 - \frac{5}{8e^3\sqrt{2}} - 2e\right)}{\pi\left(3 - e - 4e\sqrt{2}\right)}}$$

In these calculations, a structural correction factor e is taken as 0.339.

Metal foams and PCMs do not inherently exhibit a defined interfacial thermal resistance, an empirical method developed by Zhukauskas [66] is employed in the current investigation to estimate the heat transfer coefficient $(h_{sf})$ between the metal foam and the PCM.

$$h_{sf} = \begin{cases} 0.76Re_d^{0.4}Pr^{0.37}\frac{\lambda_f}{d_l} & 1 \le Re_d \le 40 \\ 0.52Re_d^{0.5}Pr^{0.37}\frac{\lambda_f}{d_l} & 40 \le Re_d \le 10^3 \\ 0.26Re_d^{0.6}Pr^{0.37}\frac{\lambda_f}{d_l} & 10^3 \le Re_d \le 2\ \times 10^5 \end{cases} \tag{35}$$

$$Re_d = \frac{\rho_f d_l\,|u|}{\mu_f}$$

$$Pr = \frac{c_{pf}\mu_f}{\lambda_f}$$

The metal foam's geometry and structure determine its specific coefficient surface area $(A_{sf})$ for thermal interaction; this is typical for open-cell foams and is calculated using Eq. (36).

$$A_{sf} = \frac{3\pi d_l\left(1 - e^{\frac{-(1-\varepsilon)}{0.04}}\right)}{\left(0.59d_p\right)^2} \tag{36}$$

Table 5 illustrates constants and variables used in the study along with their corresponding values. The mushy-zone constant controls the damping of velocity as it approaches zero when the PCM solidifies. In this study, a value of $C_{mush} = 10^7$ was selected, as it provided the closest match to the experimental melting/charging data reported by Al-Abidi et al. [67] and the numerical study performed by Palmer et al. [68], who also used RT-82 as the PCM, consistent with the present work. Previous numerical studies have shown that while the precise value of $C_{mush}$ affects the sharpness of the phase interface, values between $10^5$ and $10^7$ yield stable results without significantly altering global melting times [69–71]. The selected value therefore ensures reliable capture of the phase-change front while maintaining consistency with both experimental and established modeling practices.

### 2.4. Time-step and grid independence study

The computational model uses a quadrilateral mesh to discretize the 2D cross-section of LHTES system, as depicted in Fig. 3. To ensure that mesh resolution does not significantly influence the numerical accuracy, a mesh independence study is carried out. Three grid densities are considered: coarse (35,000 cells), medium (69,000 cells), and fine (120,000 cells). The effect of mesh resolution and time-step size on the melting behavior of the PCM in the LHTES system with T3F10 configuration is illustrated in Fig. 3 (a) and (b). The inner tube of LHTES system is fixed at 90 °C throughout the simulations. Fig. 3 (a) demonstrates that the PCM's liquid fraction varies slightly across different mesh densities, but these differences become negligible with mesh refinement. The influence of time-step size is also analyzed using three values of time steps i.e., 0.5 s, 1 s, and 2 s as illustrated in Fig. 3 (b).

**Table 5**
Constant or variables with their values used in the current analysis.

| S. No. | Constants/Variables | Values |
|---|---|---|
| 1. | $C_{mush}$ | $10^7$ |
| 2. | $B$ | 0 (liquid PCM), 1 (Solid PCM) |
| 3. | $T_w$ | 90 °C |
| 4. | $B$ | $1.381 \times 10^{-23}$ J/K |
| 5. | $\beta_k$ | $8.4407(100\varphi)^{-1.07304}$ |
| 6. | $\Phi$ | 2 percent, 4 percent, 6 percent |
| 9. | $B$ | 0, 1 |
| 10. | $A_m$ | $10^7$ |
| 11. | $\varepsilon$ | 75 percent, 85 percent, 95 percent, 98 percent |
| 12. | $d_p$ | $d_p = 0.0254$ (m)/ω (PPI) |
| 13. | $E$ | 0.339 |

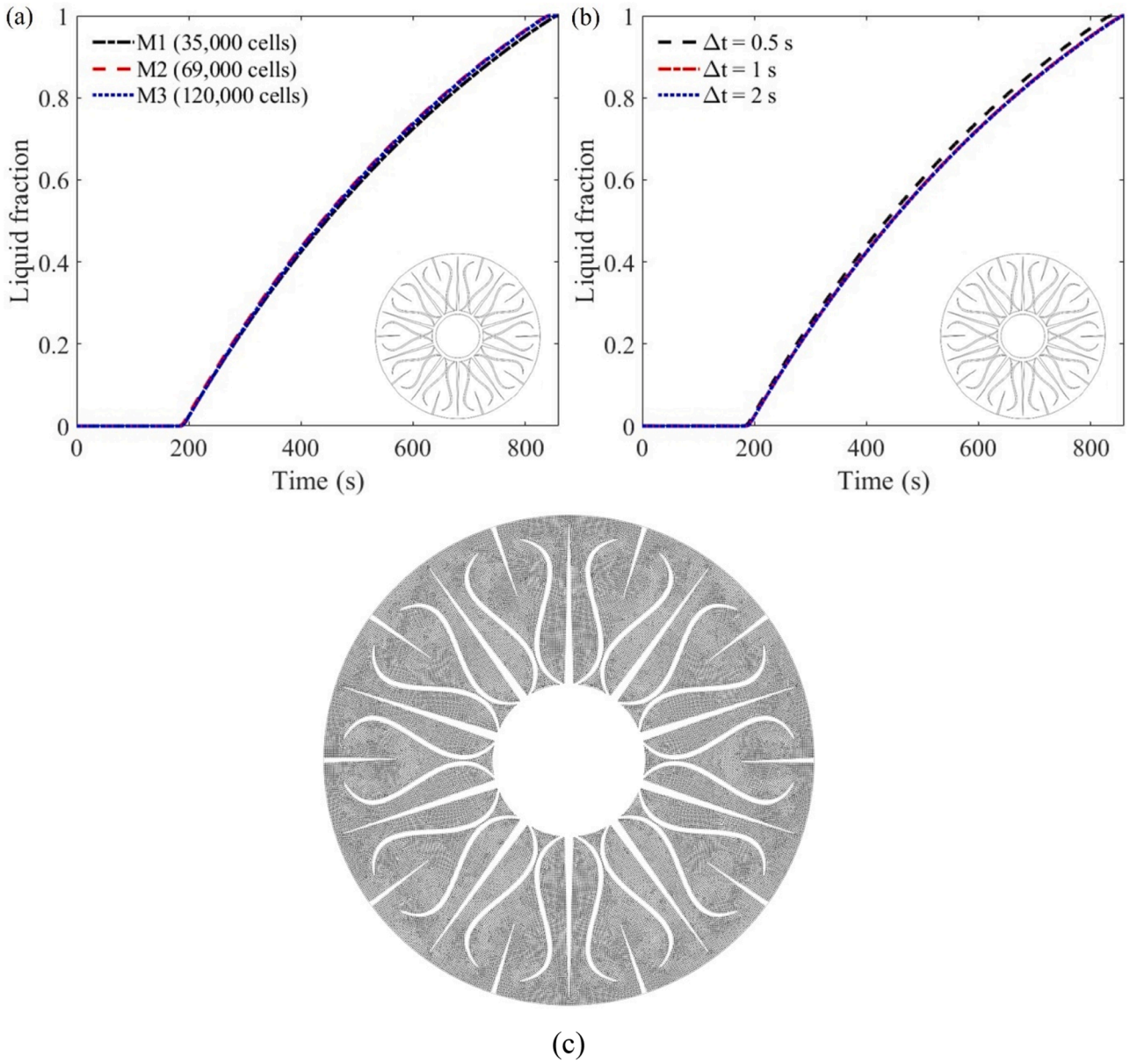


**Fig. 3.** (a) Grid-independence and (b) Time-step independence study for T3F10 fin configuration and PCM with 6% Graphene and metal foam with 75% porosity, and (c) Unstructured mesh with 69,000 cells for T3F10 fin design configuration.

Based on a balance between solution accuracy and computational cost, the mesh with 69,000 elements and a 0.5 s time step is adopted for subsequent simulations. A schematic of the computational mesh is shown in Fig. 3 (c) to illustrate the unstructured mesh distribution used in simulation.

### 2.5. Validation

The present model was validated/compared using experimental results published by Zhao et al. [49] as illustrated in Fig. 4 (a). Their study used a test configuration involving a 120 × 200 × 25 mm copper foam (95% porosity) infused with PCM (i.e., paraffin wax or RT-58). A copper plate was sintered to the foam, and a uniform heat flux was applied via an electric heating film attached to the plate's bottom surface. Temperature measurements were taken at a height of 8 mm from the heated wall. For the numerical simulation, a domain of same dimensions was discretized using a 250 × 100 uniform grid, replicating the experimental boundary conditions, initial condition and the material properties. The numerical results were then evaluated by comparing the average temperature along the y = 8 mm line to the corresponding experimental data. The close agreement between simulations and experiment supports the reliability of the developed model for further analysis.

To evaluate the reliability of the current mathematical model, the results are validated by comparing with data from an independent experimental investigation. A study conducted by Al-Abidi et al. [72], focused on analyzing the thermal behavior of a triplex-tube heat exchanger (TTHE). In their setup, the outer, middle, and inner tubes had radii of 100 mm, 75 mm, and 25.4 mm, respectively, as illustrated in Fig. 4 (b). Copper was selected for both the tubing and the fins due to its high thermal conductivity. The fins were strategically positioned to connect the inner and middle tubes, forming an enclosed region to contain the PCM. Paraffin wax (i.e., RT-82) served as PCM, with its thermal characteristics detailed in Table 2. At the start of the experiment, the PCM was completely solid at a temperature of 27 °C. Melting commenced when hot water at 90 °C was circulated through both the inner and outer tubes. For validation, the numerical model was modified

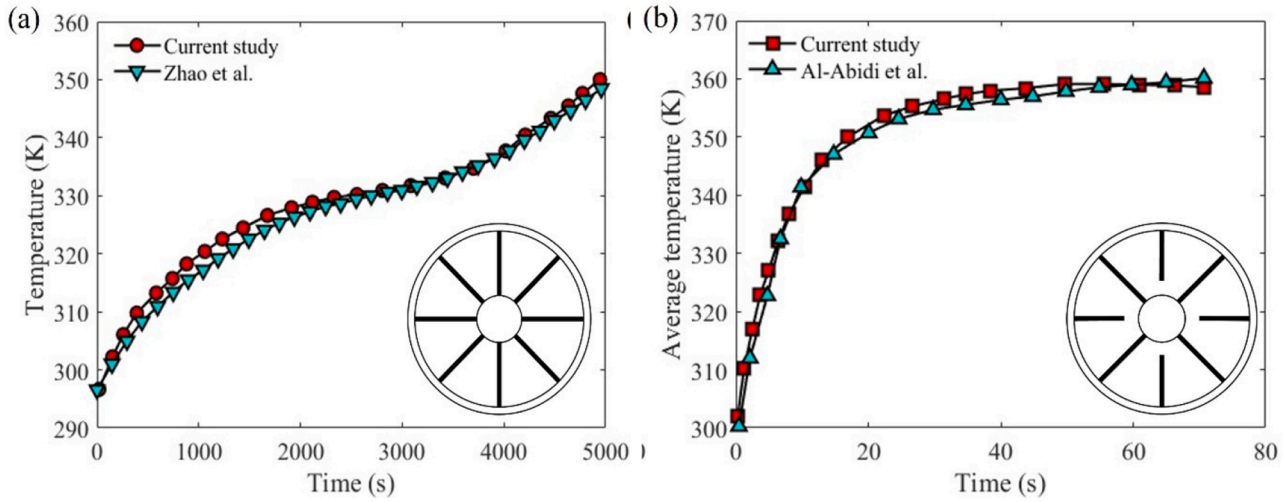


(a) Validation of the current mathematical model results with Zhao et al. [49]

(b) Validation of the current mathematical model results with Al-Abidi et al. [72]

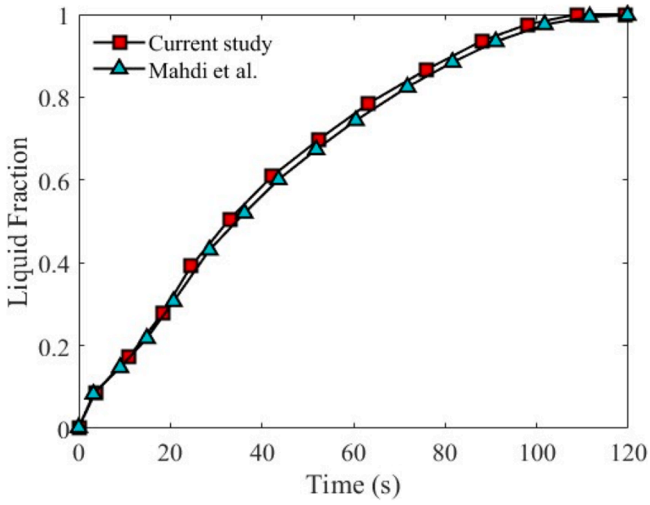


(c) Validation of the current mathematical model results with Mahdi et al. [43]

**Fig. 4.** Comparison of the current mathematical model results with the experimental studies conducted by Zhao et al. [49], Al-Abidi et al. [72] and Mahdi et al. [43].

to match the experimental geometry and boundary conditions, ensuring an accurate comparison of the results.

The boundary conditions utilized in the experimental study for the TTHE are consistently applied to the current numerical model used for validation, and the boundary conditions are as follows:

$$At\ r = r_i \rightarrow T = T_{HTF} \tag{37}$$

$$At\ r = r_m \rightarrow T = T_{HTF} \tag{38}$$

Additionally, the initial temperature conditions of the mathematical model matched those of the experimental scenario, which is as follows:

$$At\ t = 0 \rightarrow T = T_{ini} \tag{39}$$

A comparison of temperature measurements obtained from experimental thermocouples with the corresponding numerical predictions is illustrated in Fig. 4 (b). This comparison demonstrates excellent agreement, with a maximum deviation between the experimental and numerical temperatures remaining below 5%. Slight differences between experimental and simulation results are attributed primarily to inherent limitations of numerical modeling, such as the inability to fully represent complex phenomena, including the gravitational settling of solid PCM within liquid PCM.

The numerical model is further validated against the study by Mahdi et al. [43] as represented in Fig. 4 (c), who investigated melting of RT-82 PCM in a triplex-tube geometry (inner tube diameter of 50.8 mm, middle tube diameter of 150 mm, outer tube diameter of 200 mm, and length of 500 mm) with porous metal foam and nanoparticles. Validation was carried out for the case of 98% porosity copper foam with 5% nanoparticle ($Al_2O_3$) volume fraction. The predicted liquid fraction – time profiles from the present simulations showed good agreement with the numerical study performed by Mahdi et al. [43], confirming the reliability of the model.

## 3. Results & discussions

The phase transition process of PCMs in LHTES system involves a

complex interaction between natural convection and heat conduction. Understanding this combined mechanism is essential for enhancing the melting/charging efficiency of PCMs. This study explores how natural convection, non-conventional fin design configurations, and the addition of metal foams, nanoparticles and incorporating hybrid nanoparticles influence the heat transfer behavior during the melting/charging phase of LHTES system.

### 3.1. Effect of natural convection on melting/charging of LHTES system

The melting or charging performance of an LHTES system is strongly influenced by natural convection. As illustrated in Fig. 5 (a), T3 fin design configuration (see Fig. 2 (d)) is compared for two scenarios: one accounting for natural convection and another neglecting it. Fig. 5 (b) presents the corresponding liquid fraction of PCM in T3 fin configuration (see Fig. 2 (d)). The results indicate that natural convection alone significantly enhances the melting/charging process, leading to complete melting/charging approximately 1.14 times faster than in the absence of convection. This corresponds to an improvement of about 12.3% in the overall melting/charging rate. The combined influence of conduction and natural convection on the finned LHTES system is thus clearly evident from these results.

Although the fundamental roles of conduction and natural convection in PCM melting are well-established in the literature, this analysis is included to establish a baseline for the lotus-inspired fin configuration. It quantifies the specific contributions of each mechanism in this geometry and serves as a reference point for subsequent comparisons involving nanoparticles, metal foam, and hybrid systems.

Fig. 5 (b) illustrates the variation in the heat flux at the interfaces between the PCM and fins, as well as the PCM and inner pipe. The heat flux drops from nearly 60kW/m$^2$ to around 12 kW/m$^2$ within the initial 300 s, followed by a steady reduction throughout the remaining melting/charging process (i.e., from 300 s to 1440 s). The effective heat transfer coefficient between the PCM in its mushy, solid and liquid states and the heat wall, along with the temperature difference, provides an estimate of this instantaneous heat flux. Due to the low thermal conductivity of the PCM in both liquid and solid phases and the small Reynolds number of liquid PCM, and also minimum temperature gradients can substantially influence the heat flux. Furthermore, as the melting progresses, the convective flow retains some inertia, which leads to a progressive diminishing of the heat flux values over time.

Fig. 6 (a) demonstrates that the presence of natural convection significantly enhances the melting/charging rate of the PCM, especially in the upper section or region of the LHTES unit (see Fig. 5 (a) at t = 1200 s & t = 1500 s). This occurs because the direction of heat transfer opposes gravity in the upper region along with the liquid PCM moves upwards, promoting stronger convective currents. In contrast, in the lower region, where both gravity and movement of the solid PCM act in the same direction, heat conduction becomes dominant. Vortex structures emerge within the liquid PCM near the fins due to substantial temperature gradients between the fins and surrounding PCM, as illustrated in Fig. 6 (c). Initially, these vortices are very small due to high viscosity of the PCM but grow larger as the melting progresses (see Fig. 6 (a) at t = 1200 s & t = 1500 s). The vortices formed in the upper region of the liquid PCM portion tend to be larger than those in the lower region. Over time, these vortices expand and merge, further intensifying convective motion. Therefore, the upper region of the LHTES system is primarily influenced by natural convection, while the lower section is governed by mainly conduction and also by convection at t = 1200 s and 1500 s. Enhancing the melting or charging efficiency of LHTES systems thus requires an optimized balance between conduction and convective heat transfer mechanisms.

Fig. 6 (b) illustrates the influence of natural convection on the temperature distribution within the LHTES system. When natural convection is active, temperature gradients are more uniformly distributed, resulting in a higher overall heat transfer rate compared to purely conductive conditions. This improvement occurs because buoyancy-driven flow enhances the circulation of molten PCM, which accelerates energy transport away from the heated walls and toward the unmelted regions. The increased fluid motion and increase in the liquid PCM also strengthen the temperature gradient at the solid-liquid interface, which reduces the effective thermal resistance between the fins and the PCM. As melting progresses, this mechanism leads to faster heat penetration, particularly in the upper part of the storage unit where convective currents rise and dominate the transport process. Conversely, the lower region remains more conduction-controlled due to the alignment of gravity and solid PCM, which restricts convective circulation. A more uniform melting behavior can be achieved by designing the fin arrangement and thermal pathways to maximize the beneficial effects of natural convection while complementing it with conduction where

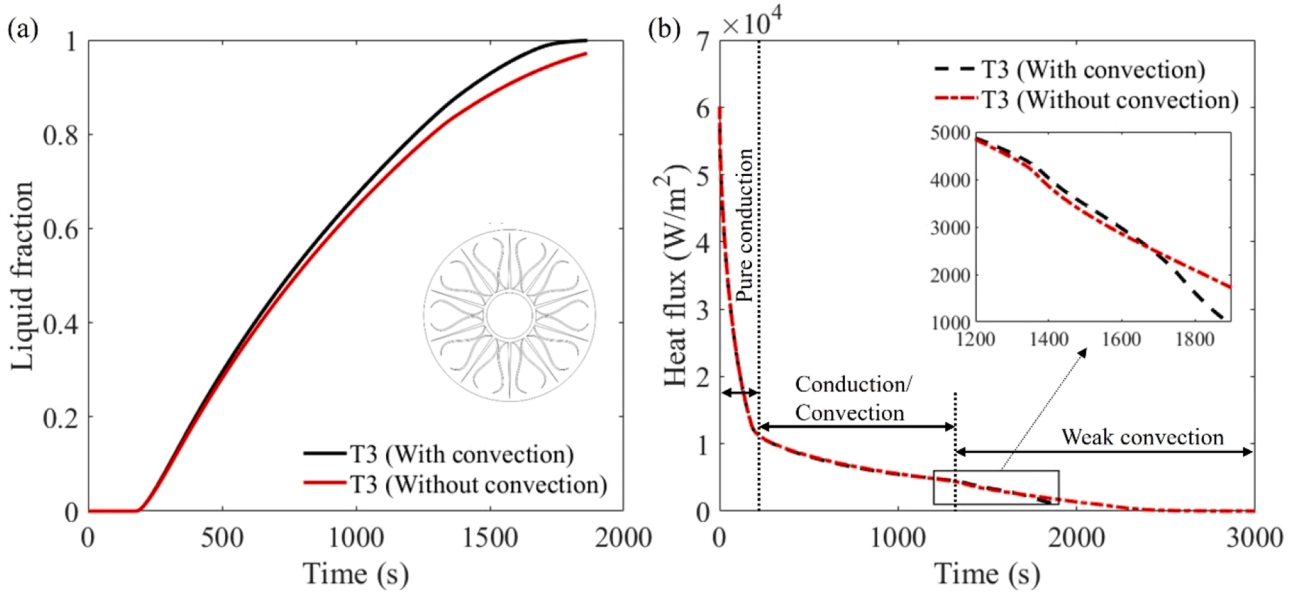


**Fig. 5.** Impact of natural convection in the LHTES system (a) Effect of convection on the melting/charging behavior of PCM for T3 fin configuration (b) Variation of the heat flux in PCM during melting/charging.

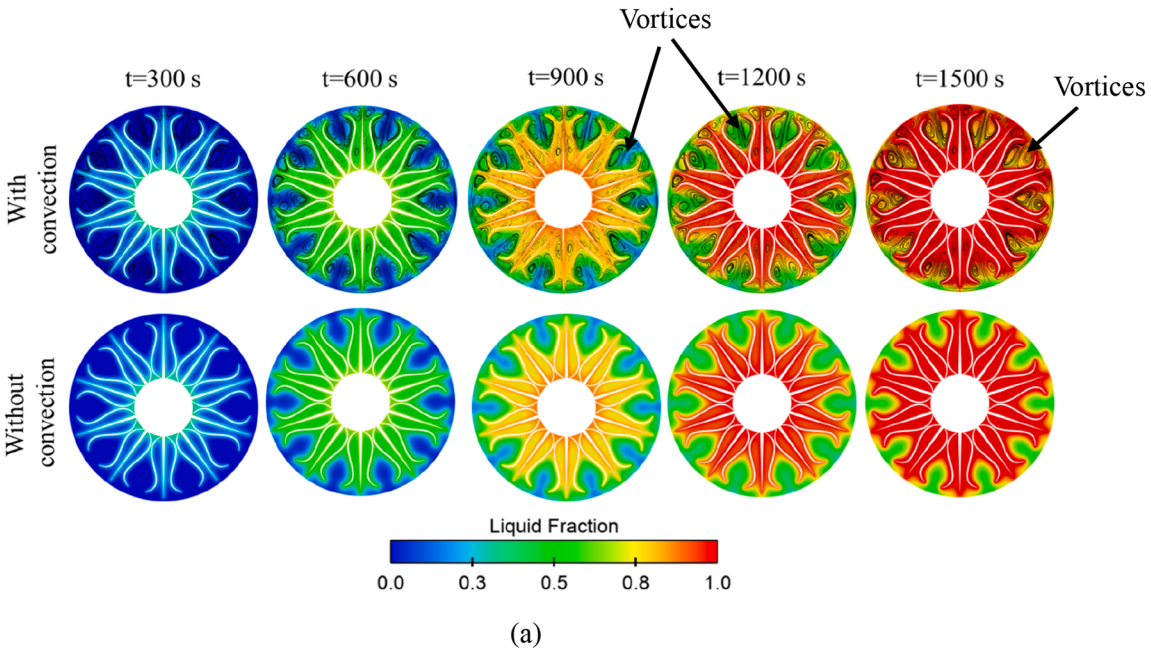


(a)

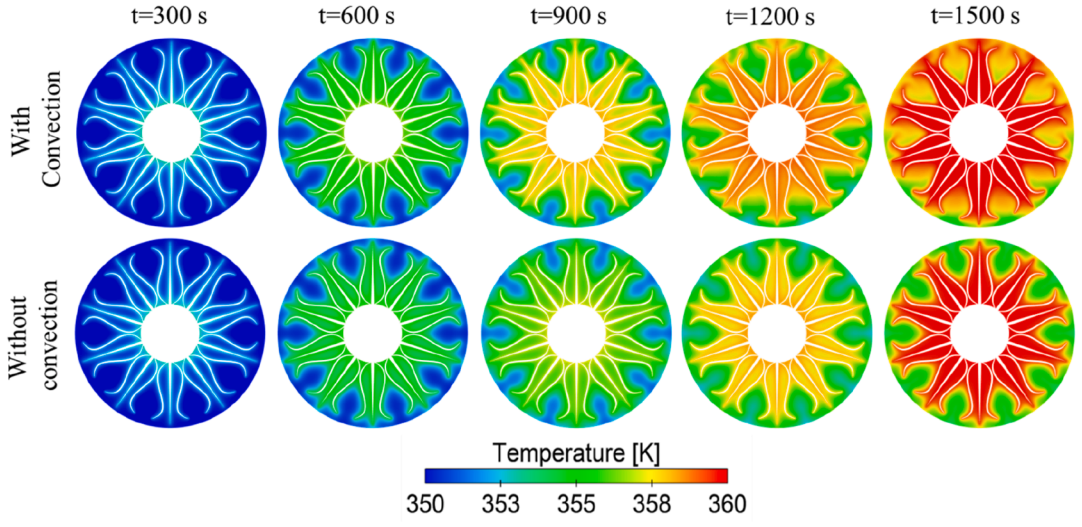


(b)

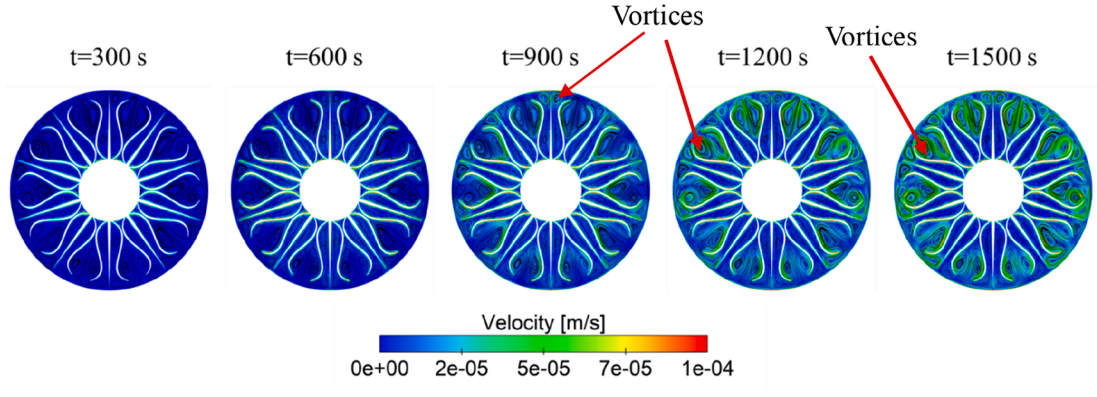


(c)

**Fig. 6.** (a) Liquid fraction contour of T3 fin design configuration including natural convection, (b) Effect of natural convection on the temperature distribution in T3 configuration, and (c) Velocity and stream line for T3 fin design configuration at different time steps.

convective flow is limited. Such optimization is crucial for improving both the charging rate and the discharging rate along with the thermal efficiency of LHTES systems. Fig. 6 (c) represents the velocity contours with superimposed streamlines showing natural convection flow structures during PCM melting for the T3 configuration. Low-velocity zones (blue) dominate near the solid PCM, while higher velocity recirculations (green - yellow) develop in the melted regions adjacent to the heated walls and fins. As melting progresses, buoyancy-driven vortices form near fin tips and grow in size and strength, particularly in the upper region, where opposing gravity enhances upward liquid motion. These vortices merge and intensify with time, indicating that convection increasingly governs heat transfer in the upper PCM domain, while conduction remains dominant in the lower region.

### 3.2. Impact of different non-standard fin design configurations on melting/charging

Fig. 7 (a) illustrates the melting/charging performance of the LHTES system analyzed for various fin configurations with natural convection. The total melting times ranged from 1747 s to 4727 s, with the slowest melting/charging occurring in configuration T3S4 (i.e., (4727 s)), which employed sparsely spaced fins; this configuration is used in this study as the baseline for comparison. High-density fin design configurations, such as T3F4 and T3F10, completed melting/charging in 1747 s, representing an improvement of approximately 63% relative to T3S4. Similarly, T3F2, with a melting/charging time of 1772 s, achieved a 62.5% reduction in melting/charging time, while the uniform fin design configuration (i.e., T3) showed a 60.6% reduction, corresponding to 1864 s. Moderately improved designs such as T1 & T2 reduced melting/charging time by approximately 54% (2159 s) - 55% (2207 s) compared to T3S4, whereas T1NF (having a melting/charging time of 2507 s), T2NF (with melting/charging time of 2618 s) and T3NF (took 2181s to fully melt) achieved 47% - 44% improvements. Designs with angular fins (i.e., T3A4 (4401 s), T3A6 (3226 s), T3A8 (2276 s) and sparse fins (T3S6 (3086 s), T3S8 (2218 s) showed moderate to least performance, with approximately 6% - 52% improvements over the baseline (i.e., T3S4). The results indicate that configurations with densely distributed fins maximize conduction heat pathways, while designs with sparse or angular fins exhibit thermal non-uniformities and suppressed convective circulation, prolonging the melting/charging process. Comparisons between natural convection enabled designs (T1 - T3) and the same fin design configuration without fins (i.e., T1NF–T3NF) further confirm that buoyancy-driven flow significantly accelerates melting/charging, with T3 outperforming T3NF by approximately 14.5%. These findings demonstrate that coordinated enhancement of conduction (via fin density) and convection (via buoyancy effects) can substantially reduce melting/charging time.

Compared with conventional straight fins, the lotus-shaped fin structure offers significant advantages. Straight fins or conventional fins generally accelerate PCM melting/charging by extending conduction paths, but their simple geometry produces localized thermal dead zones, limited surface area, and restricted natural convection, which collectively slow down the overall melting–solidification process. As a result, the enhancement achieved with straight fins typically falls in the range of 25% – 40%, depending on fin spacing and orientation [18,73,74]. More advanced but still standard geometries, such as multi-branch or tree-shaped fins, have been reported to reduce melting/charging time by ~ 34 – 45 % relative to rectangular plain fins [21,73]. Other optimized arrangements, such as longitudinal fins in triplex-tube LHTES units, have shown 59–86% faster charging/melting when combined with nanoparticles [75], while corrugated fin designs have demonstrated superior melting/charging uniformity compared with rectangular plain fins under similar conditions [76]. In contrast, the lotus-shaped fin design was chosen for this study because its radially distributed branches increase the effective heat transfer surface, eliminate thermal dead zones by distributing heat more uniformly, provide a higher surface-to-volume ratio that enlarges the effective conduction pathways, and enhance buoyancy-driven circulation rather than suppressing it. Consequently, the lotus-shaped fins design reduced melting/charging time up to ~ 45% – 63%, with the best cases (T3F4 and T3F10) achieving 1747 s compared with 4727 s for the sparse-fin baseline (T3S4). These results demonstrate that the lotus-shaped design not only overcomes the inherent limitations of conventional straight fins but also achieves quantitatively superior performance compared with values reported in the literature.

Fig. 7 (c) and 7 (d) present the average temperature increase and total energy stored profiles of PCM for the 15 different fin configurations during the melting/charging process. The total energy stored in PCM as presented in Fig. 7 (d) shows a monotonic increase, with the slope indicating the charging/melting rate and the plateau corresponding to complete melting/charging. Using 80% of the total energy ($\approx 2.4 \times 10^5$ J/kg) as a benchmark, high dense fin design configurations (i.e., T3F4, T3F10) reach this threshold in approximately 1747 s, which is nearly 55 - 60% faster than sparse fin arrangements (i.e., T3S4), which require roughly 4727 s. Fin design configurations, i.e., T3F2 and T3, achieve 80% melting in 1772 s – 1864 s, representing an improvement of about 45% over the slowest configuration (i.e., T3S4 fin design configuration). Basic uniformly spaced fins, T1 and T2, fall in the intermediate range, achieving the benchmark of melting of PCM in approximately 2159 – 2207 s, while sparse or angular configurations, T3S4 and T3A4 extend beyond 4401 – 4727 s, reflecting the lowest melting/charging efficiency. The trends in Fig. 7 (c) demonstrated that higher fin density produces a steeper temperature rise, indicating enhanced conductive heat transfer and improved synergy with buoyancy-driven convection in the upper portion of the PCM domain. Conversely, sparse or angular fins promote non-uniform thermal fields and slower heat transfer towards the PCM in the solid phase. These results confirm that increasing the number of fins and optimizing their distribution significantly reduces charging/melting time and improves thermal performance, achieving up to a 60% reduction in melting/charging duration compared to suboptimal designs, such as T3S4, T3S6, T3A4 and T3A6.

Fig. 8 illustrates the liquid fraction distributions for different fin configurations in the LHTES system at 1200 seconds, providing insight into the intermediate stage of melting/charging progression. During the initial melting/charging phase, all configurations exhibit similar liquid fractions (~ 0.25 - 0.30) except for T3S4, T3A4, T3S6 and T3A6 since conduction through the fins dominates heat transfer and natural convection effects remain limited. As melting proceeds, differences emerge; i.e., high-fin-density configurations such as T3F4 and T3F10 achieve liquid fractions of approximately 0.75 – 0.80, indicating rapid heat transfer and improved uniformity. Other fin design configurations, including T3 and T3F2, reach liquid fractions of about 0.60 - 0.65, reflecting balanced contributions from conduction and buoyancy-driven convection. Basic uniformly spaced fin configurations (T1, T2, T1NF and T2NF) achieve around 0.50 - 0.55, while sparse or angular fin configurations (T3S4, T3A4, T3S6 and T3A6) trails with liquid fractions near 0.40 - 0.45, illustrating slower melting/charging and localized heat transfer near the heated PCM. These results confirm that fin density and geometry critically influence the transition from conduction-controlled to convection-enhanced melting/charging, with denser fin layouts enabling more uniform and accelerated phase change throughout the PCM domain.

The comparative melting/charging times in Fig. 7 (b) highlight how fin thickness, orientation, and density influence thermal performance. Among the baseline sets, T3 (1864 s) performed best compared to T1 (2159 s) and T2 (2207 s), as its geometry provides shorter conduction pathways and promotes stronger buoyancy-driven circulation. When the fins were removed, performance worsened, measured as melting/charging time in this case, (T1NF = 2507 s, T2NF = 2618 s, T3NF = 2181 s), since these variants reduced fin perimeter and weakened convective interaction. Sparse fin layouts (T3S4 = 4727 s) and low-angle geometries (T3A4 = 4401 s) had the slowest melting/charging due to

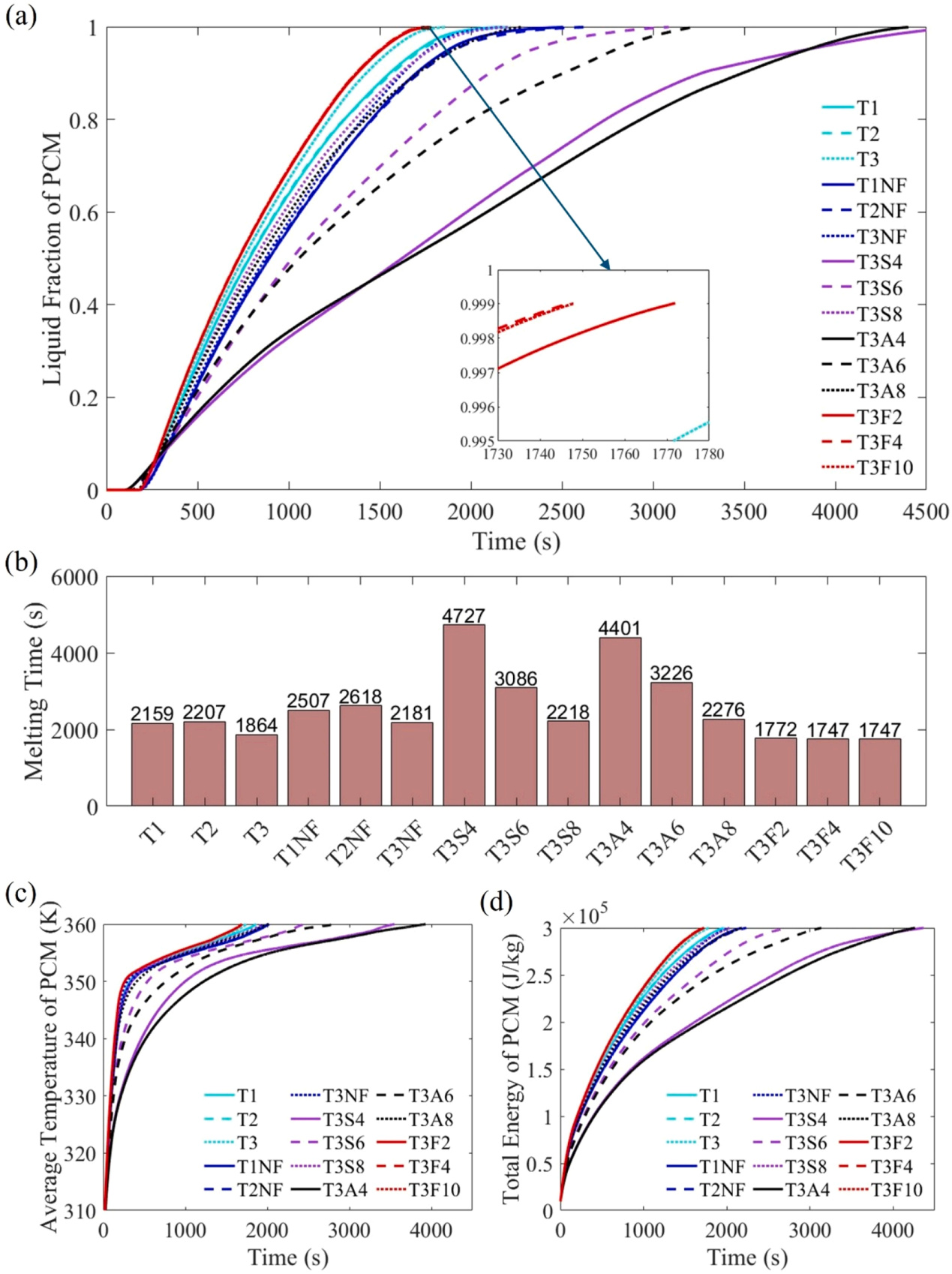


**Fig. 7.** (a) Liquid fraction of PCM, (b) Total melting time of PCM for different fin configurations, (c) Average temperature, and (d) Total energy of the PCM.

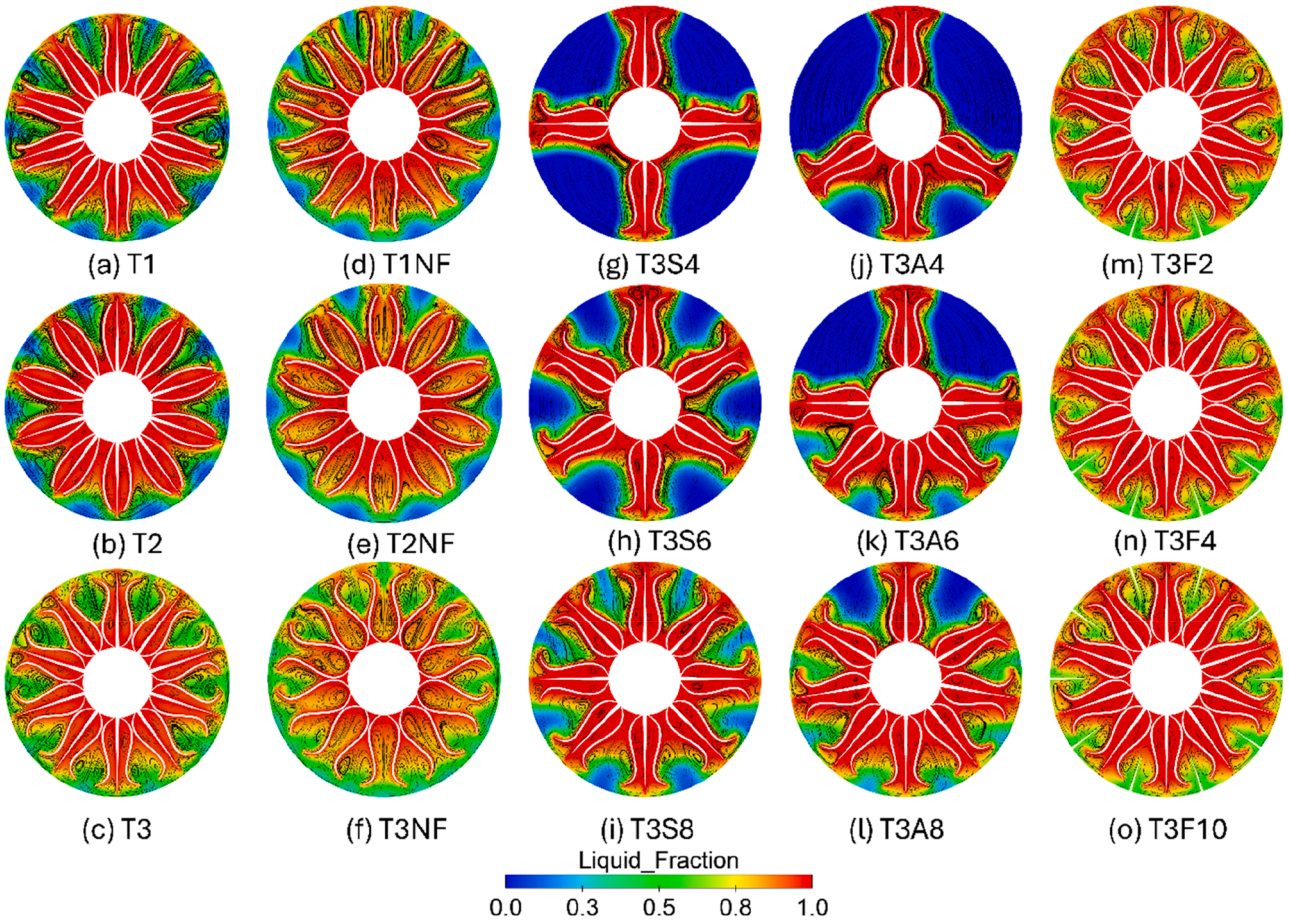


**Fig. 8.** Liquid fraction contours with streamline during the melting/charging process of PCM for the 15 different non-standard fin design configurations at 1200 seconds.

wide spacing that left large PCM volumes conduction-dominated. Increasing fin number improved results: T3S6 (3086 s) and T3S8 (2218 s) shortened melting/charging time as more surfaces enhanced conduction and triggered stronger circulation. Similarly, angled fins at moderate density (T3A6 = 3226 s, T3A8 = 2276 s) improved performance relative to T3A4, as better orientation distributed heat more evenly and coupled with natural convection. The highest-performance designs were high-perimeter fins (T3F2 = 1772 s, T3F4 = 1747 s, T3F10 = 1747 s), which reduced melting/charging times by ~63% relative to T3S4. These designs provided multiple thin conduction pathways and encouraged the formation of multiple convection zones. However, the similarity in melting/charging time between T3F4 and T3F10 indicates diminishing returns at high fin density due to PCM displacement, which reduces energy storage capacity. Overall, these results demonstrate that geometric optimization requires balancing between increased fin perimeter and density with preserved PCM volume. Optimal fin designs, such as T3F4, maximize perimeter-to-volume ratio while maintaining strong conduction–convection coupling without excessive PCM loss.

While it is well established that increasing the number of fins enhances conductive pathways and accelerates PCM melting/charging, this improvement comes at the expense of reduced PCM volume and increased material cost. For a fairer comparison, optimized designs should also be evaluated under the same number of fins. In this context, the results show that even when fin number is fixed, the geometry and distribution strongly impacts the performance. For example, designs such as T3F4 and T3F10 (high perimeter, optimized layouts) achieved melting times of 1747 s, which are significantly shorter than alternative layouts with comparable fin counts but less effective orientations (e.g., T3S6 or T3A6, 3086–3226 s). This indicates that fin orientation, thickness, and perimeter distribution play a decisive role in optimization beyond simply increasing the number of fins.

### 3.3. *Effect of nanoparticles and hybrid nanoparticles on the melting/charging performance*

Based on the melting/charging time and influence of natural convection, T3F10 fin design configuration sees T3F10 LHTES system in Fig. 2 (d) was selected to analyze the impact of nanoparticles at varying volume fractions. Fig. 9 (a) and (e) respectively compare the liquid fraction and total energy during melting/charging for CNT and graphene nanoparticles at 2%, 4%, and 6% volume fractions. The liquid fraction graphs in Fig. 9 (a) indicate progressive melting/charging for all cases, with graphene-based nano-PCM consistently achieving faster melting/charging than CNT-based nano-PCM due to graphene's higher thermal conductivity. The melting time data in Fig. 9 (c) shows this improvement. Using 2% CNT as a baseline leads to a melting/charging time of approximately 1734 s, whereas graphene with a volume fraction of 2% reduces the melting/charging time to 1678 s, corresponding to a 3.2% improvement. Increasing graphene concentration further lowers melting/charging times to 1647 s at 4% (~5% improvement) and 1614 s at 6% (~6.9% improvement). In comparison, CNT shows negligible improvement with increasing concentration. The melting/charging times for 4% CNT (1760 s) and 6% CNT (1783 s) are slightly longer than the 2% CNT baseline (1734 s), indicating a delayed rather than an accelerated melting/charging. This slower melting/charging can be attributed to CNT agglomeration and increased viscosity at higher volume fractions, which suppress natural convection and reduce overall

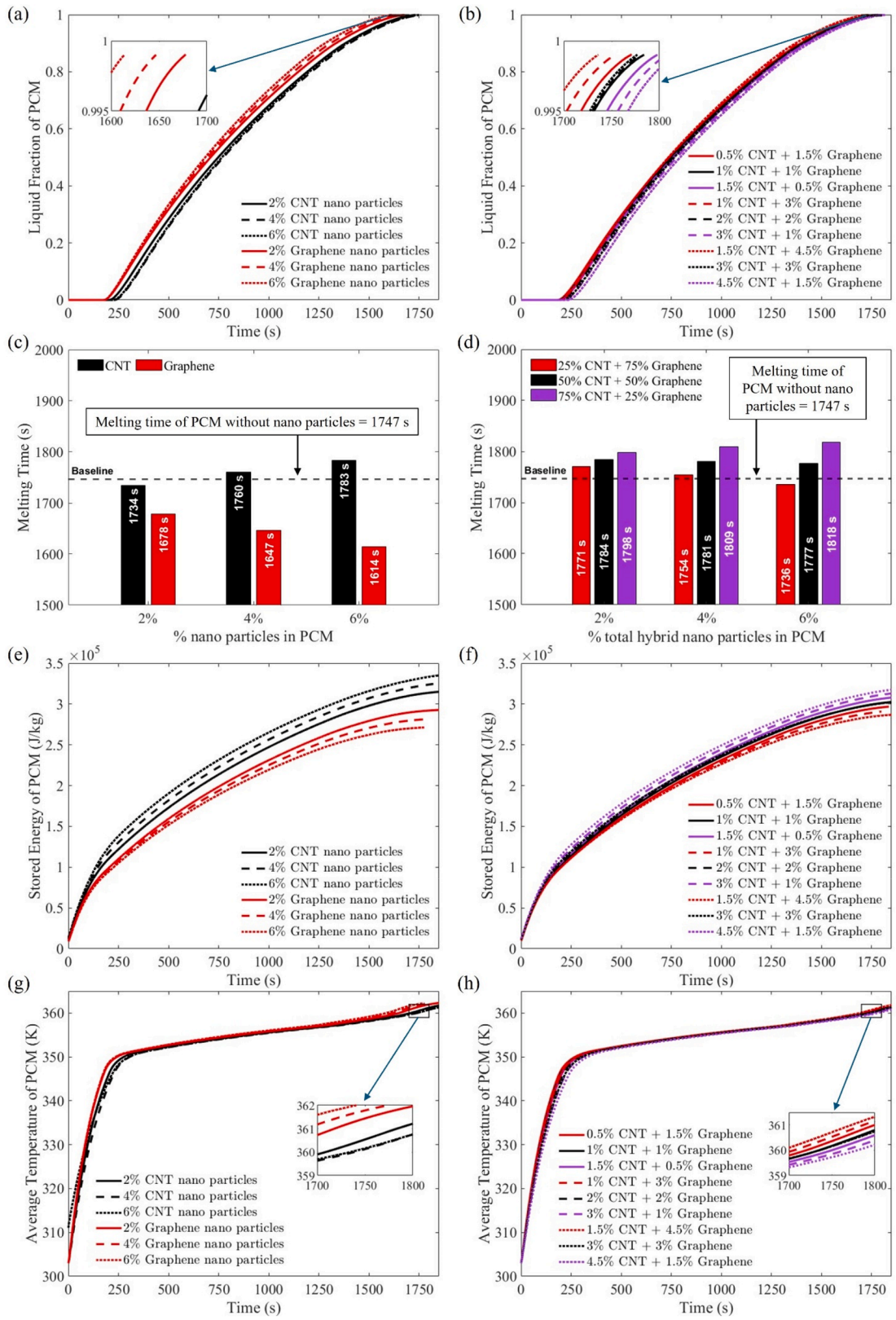


**Fig. 9.** Effect of nanoparticles (left) and hybrid nanoparticles (right) on the melting behavior of PCM under the T3F10 fin configuration (a) Liquid fraction with single nanoparticle (b) Liquid fraction with hybrid nanoparticles, (c) Total melting time of PCM with different concentrations of individual CNT and graphene nanoparticles, (d) Total melting time of PCM with hybrid nanoparticles (CNT + graphene), (e) Total energy versus time for various concentrations of individual CNT and graphene nanoparticles in PCM, (f) Total energy versus time for hybrid nanoparticles (combinations of CNT and graphene) in PCM, (g) Average temperature of the PCM versus time with different volume fractions of individual nanoparticles, and (h) Average temperature of the PCM versus time with different for hybrid nanoparticles (combinations of CNT and graphene).

heat transfer efficiency. Energy profiles in Fig. 9 (e) confirm this trend, where graphene-based PCMs reach higher stored energy levels earlier during melting/charging. The superior performance of graphene is attributed to its higher thermal conductivity-to-size ratio, which enhances heat transfer at equivalent volume fractions. This observation is consistent with the theoretical relationship described in Eq. (15), which predicts that the thermal conductivity of nano-enhanced PCMs is inversely proportional to particle diameter, and aligns with experimental findings reported by Ravikanth et al. [77]. Overall, graphene nanoparticles achieve melting/charging rates approximately 1.03 times faster at 2% concentration, 1.07 times faster at 4% concentration, and 1.08 times faster at 6% concentration compared to CNT, making them a more effective option for enhancing the charging/melting process in LHTES systems.

Fig. 9 (b) illustrates the performance of hybrid CNT–graphene nanoparticles on PCM melting/charging behavior at total nanoparticle volume fractions of 2%, 4%, and 6%. The liquid fraction trends in Fig. 9 (b) indicate a gradual increase across all hybrid ratios, with only minor variations among different CNT-to-graphene proportions. Unlike graphene systems, which demonstrated faster melting/charging rates, the hybrid configurations exhibit slightly lower performance than both CNT and graphene cases at equivalent volume fractions. The melting/charging time results in Fig. 9 (d) confirm this observation. At a 2% volume fraction, the hybrid proportion of CNT and graphene requires 1771 – 1798 s to fully melt the PCM, while pure CNT and graphene systems complete melting in approximately 1734 s and 1678 s, respectively. At a 4% concentration, hybrids' proportion of CNT and graphene takes 1754 – 1809 s, compared to 1760 s for CNT and 1647 s for graphene. A similar trend is observed at 6% concentration, where hybrids melt in the range of 1736 - 1818 s, while CNT and graphene take 1783 s and 1614 s, respectively. This clearly shows that hybrids consistently exhibit slower melting/charging than either single nanoparticle. The slower performance of hybrids is attributed to the non-additive thermal conductivity behavior when CNT and graphene are combined. The different morphologies and aspect ratios of CNT (tubular) and graphene (planar) result in inefficient percolation pathways and reduced interfacial contact networks, which limit conductive heat transfer improvements. Additionally, hybrid dispersions are more prone to agglomeration, reducing the effective heat transfer surface area. As a result, even when graphene is present in the hybrid mixture, the overall thermal conductivity remains lower than that of pure graphene, leading to longer melting/charging times. The total energy graph in Fig. 9 (f) also supports this conclusion. Hybrid CNT–graphene nanoparticles in PCM exhibit a noticeably lower energy charging/melting rate throughout the melting/charging process, as evidenced by the reduced slope of their total energy time curves compared to pure nanoparticles. This reduction in slope reflects a slower heat absorption rate, consistent with their delayed liquid fraction growth. Even hybrids with higher graphene content fail to achieve the early energy rise and rapid saturation observed in pure graphene-enhanced PCMs, which reach peak energy storage more quickly due to superior thermal conductivity and stronger convective–conductive coupling. The indicates that the combination of CNT and graphene does not create synergistic thermal pathways; instead, mismatched particle geometries and interfacial resistances disrupt percolation networks and limit effective heat transfer. Consequently, hybrid nanoparticle dispersions provide diminished energy storage kinetics relative to single-nanoPCM, particularly graphene-based PCMs. Figs. 9 (g) and (h) show the temporal evolution of the average PCM temperature for CNT-, graphene-, and hybrid-enhanced systems under the T3F10 fin configuration. Across all cases, three stages can be observed: (i) an initial rapid temperature rise during the early melting/charging period (0–300 s), (ii) a slower growth region where latent heat absorption dominates (300–1200 s), and (iii) a final saturation stage as the PCM approaches complete melting/charging (beyond 1200 s). In the early stage, conduction through the fins governs heat transfer. Graphene-enhanced PCMs exhibit a faster initial rise compared to CNT and hybrid cases, owing to graphene's higher intrinsic thermal conductivity and smaller particle size, which improve thermal diffusion pathways. During the intermediate phase, as liquid PCM accumulates around the fins, buoyancy-driven convection strengthens. Graphene systems sustain steeper temperature growth, confirming that higher effective conductivity also enhances natural convection. By contrast, CNT-based PCMs, particularly at higher concentrations (4–6%), show slower temperature increases and ultimately increases the melting time. This delay is again attributed to particle agglomeration and increased viscosity, which suppress convective circulation and reduces heat transfer efficiency. In the final stage, the temperature asymptotically approaches equilibrium. Graphene PCMs consistently reach this plateau earlier than CNT and hybrid mixtures, which lag due to weaker conductive and convective coupling. The results align with the melting/charging time and energy storage data in Figs. 8 (a–f), reinforcing that graphene nanoparticles provide the most effective enhancement in finned LHTES systems.

Fig. 10 presents the liquid fraction contours for the T3F10 configuration with 6% graphene nanoparticles at different time intervals during melting/charging. The contours demonstrate a clear progression from conduction-dominated melting/charging in the early stage (blue to green regions) to convection-enhanced melting/charging in the later stage (yellow to red regions). Initially, melting/charging begins uniformly around the fin surfaces due to high local thermal gradients, with the liquid fraction concentrated near the fin–PCM interfaces. As melting/charging progresses, buoyancy-driven natural convection becomes more pronounced, forming distinct plume-like flow structures between adjacent fins, which accelerate heat transfer toward the central PCM region. By the final stage, nearly complete melting/charging (i.e., liquid fraction $\approx 1.0$) is achieved, with a uniform red color signifying a fully liquid state. When compared to other configurations and nanoparticle enhancements, this T3F10 with 6% graphene exhibits the highest melting/charging rate and energy storage performance. The high fin density (i.e., T3F10 fin design configuration) maximizes conductive pathways, while graphene nanoparticles significantly enhance the thermal conductivity and convective heat transfer by reducing the PCM's thermal resistance.

### 3.4. *Effect of metal foam on melting/charging performance*

Fig. 11 illustrates the effect of metal foam porosity combined with varying graphene nanoparticle volume fractions of 2%, 4%, and 6% on the melting/charging characteristics of the PCM. As can be appreciated in Fig. 11 (a), for pure PCM, the influence of foam porosity is clear: at a porosity of 0.75, the liquid fraction reaches full melting/charging in approximately 17 minutes, whereas at 0.98 porosity, the same process takes around 1860 s. Lower porosity reduces the void space within the foam and increases the available surface area for conduction, enabling heat to transfer more efficiently from the foam to the PCM. Since copper foam possesses significantly higher thermal conductivity than the PCM, decreasing porosity enhances heat transfer pathways and accelerates melting/charging. Fig. 11 (b) to 11 (d) demonstrates that introducing graphene nanoparticles into the PCM further improves melting/charging performance at each porosity level. At 2%, 4%, and 6% nanoparticle volume fractions, the liquid fraction curves consistently shift upward, indicating faster melting/charging than pure PCM. Among the porosity levels, $\varepsilon = 75\%$ achieves the fastest melting/charging for all nanoparticle loadings, whereas $\varepsilon = 98\%$ remains the slowest in terms of melting/charging time due to reduced conductive pathways and higher PCM volume within the voids but it shows that a small fraction of high conductivity material produces a high benefit (when compared with pure PCM). Increasing the nanoparticle volume fraction from 2% to 6% reduces total melting/charging time because graphene nanoparticles raise the effective thermal conductivity of the PCM and improve convective–conductive coupling during melting/charging. The combined effect of lower porosity and higher nanoparticle concentration yields a

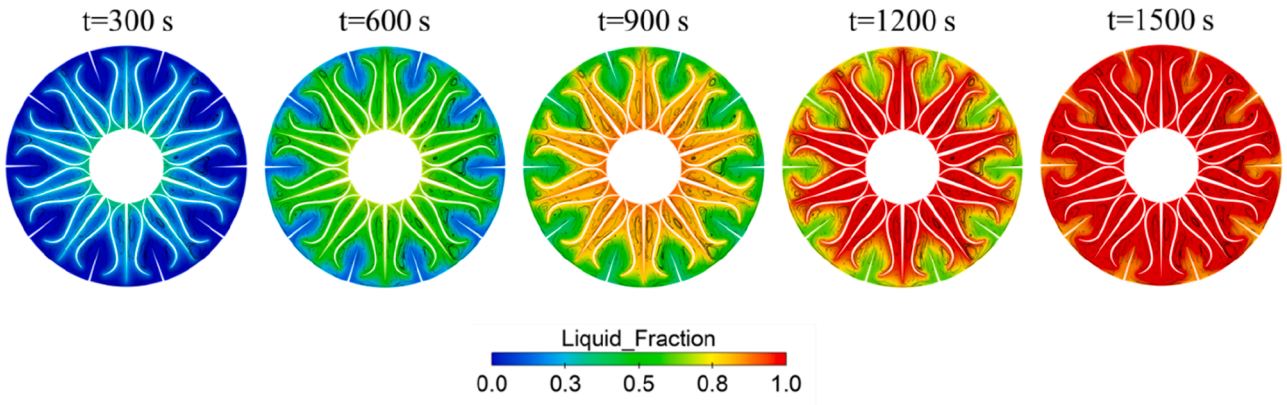


**Fig. 10.** Liquid fraction contours of T3F10 fin design configuration with 6% graphene.

reduction in the melting/charging time, nearly halving the duration compared to pure PCM without foam. These results align with earlier findings and validate the role of nanoparticle size: smaller graphene particles, with their larger surface area-to-volume ratio, enhance heat transfer more effectively than larger particles. This behavior agrees with Eq. (15), which predicts an inverse relationship between nanoparticle diameter and effective thermal conductivity, and is consistent with the experimental observations reported by Ravikanth et al. [77], where larger nanoparticles tend to settle faster, reducing uniformity and heat transfer efficiency. Fig. 11 (e) shows the heat flux variation during the melting/charging process for the LHTES system using 98% porosity metal foam combined with graphene-enhanced PCM in T3F10 fin configuration. The melting/charging behavior transitions through three regimes: pure conduction (0 – 250 s), conduction-convection transition (250 – 850 s), and weak convection (850 – 1250 s). In the initial conduction phase, heat flux peaks at around $6 \times 10^4$ W/m$^2$ due to high thermal gradients at the solid - liquid interface. Although the foam improves heat transfer compared to pure PCM, the high porosity (98%) limits solid contact between foam struts and PCM, reducing conductive pathways and slowing heat transfer relative to low-porosity foams (e.g., 75%). During the conduction - convection phase, melting accelerates as buoyancy-driven plumes develop in the liquid PCM, assisted by the high thermal conductivity of graphene nanoparticles. However, the large void volume at 98% porosity means more PCM will be melt/charge, prolonging the process despite enhanced convective mixing. In the final weak convection stage, heat flux decreases to low values ($<0.5 \times 10^4$ W/m$^2$) as nearly all PCM becomes liquid and thermal gradients diminish. This behavior highlights the trade-off at 98% porosity: greater PCM volume is preserved for energy storage, but melting/charging is slower due to reduced foam conduction and higher PCM content compared to lower-porosity designs. Fig. 12 (a) presents the temporal evolution of the liquid fraction for the LHTES system using metal foam with 98% porosity and 6% graphene-enhanced PCM for the T3F10 fin configuration. The contours illustrate the melting/charging front progression at successive time intervals, transitioning from conduction-dominated behavior to convection-enhanced melting. At the early stage (t = 300 s), melting/charging initiates at the fin–PCM interfaces, where heat flux is the highest, leading to localized liquid zones (blue transitioning to green). The high porosity of 98% results in a larger void volume filled with PCM, which limits solid–solid contact between the foam and PCM and reduces conductive heat transfer pathways. Consequently, melting/charging progresses slowly in the initial phase, and natural convection currents are weakly developed due to insufficient liquid fraction. After t = 600 seconds, as the melt fraction increases (green to yellow zones), buoyancy-driven convection intensifies within the PCM, forming plume-like patterns illustrated between fins. These plumes enhance mixing in the upper portions of the storage domain, accelerating melting/charging in localized regions but leaving the lower section governed by conduction. In the later stages (t = 900 s), the majority of the PCM transitions to the liquid phase, with residual solid pockets persisting near the core due to the reduced thermal conductivity of high-porosity foam and the longer conduction path required for complete melting/charging. Full melting/charging is achieved significantly later compared to low-porosity cases (e.g., 75%), despite the presence of graphene nanoparticles, because the increased void fraction diminishes the conductive benefit of the foam. This highlights the trade-off between maximizing PCM volume (high porosity) and ensuring efficient heat conduction (low porosity) in optimizing LHTES system performance. The velocity contours with streamlines shown in Fig. 12 (b) correspond to the T3F10 fin configuration integrated with 6 % graphene-enhanced copper foam at 98 % porosity. The velocity field indicates the presence of multiple, symmetric recirculating vortices established between adjacent fins, which arise from localized buoyancy-driven motion and fluid–solid interactions within the porous medium. Although the absolute velocity magnitudes remain low, the formation of coherent vortex structures demonstrate enhanced fluid mixing within the inter-fin region. This dynamic behavior is particularly important in such highly porous metal foams, where conduction through the solid copper–graphene matrix dominates heat transfer, but secondary convective contributions provided by weak vortex circulation further accelerate energy transport and thermal homogenization. The addition of graphene increases the intrinsic thermal conductivity of the solid network, while the high porosity of the foam ensures minimal flow resistance and preserves open channels for recirculatory motion. Collectively, this hybrid conduction–convection mechanism improves overall thermal performance, reduces localized thermal resistance, and promotes uniform temperature distribution across the finned domain, which is critical in compact heat exchanger and latent heat thermal energy storage applications, (Table 6).

### 3.5. Performance enhancement

Beyond faster melting/charging, the optimized lotus-inspired fins improve spatial uniformity of the phase change. We quantified uniformity by computing the standard deviation ($\sigma$) of liquid fraction ($\sigma_{LF}$) and temperature ($\sigma_T$) across monitoring points distributed in the PCM domain (see Fig. 13 for probe locations). At matched intermediate charging/melting stages, the lotus design T3F10 yields $\sigma_{LF} = 0.0095$ at t = 600 s (mean liquid fraction ($\bar{f}_l$)=0.274), whereas the sparse straight-fin baseline T3S4 shows $\sigma_{LF} = 0.10$ at t = 2280 s (mean $\bar{f}_l = 0.304$), corresponding to an ~ 90% reduction in spatial variability. Temperature statistics follow the same trend, with consistently lower $\sigma_T$ values for lotus fins at the same global melt/charge progression. These results confirm that lotus-inspired fins suppress stagnation zones and promote a more homogeneous phase-change process compared to conventional straight-fin geometries.

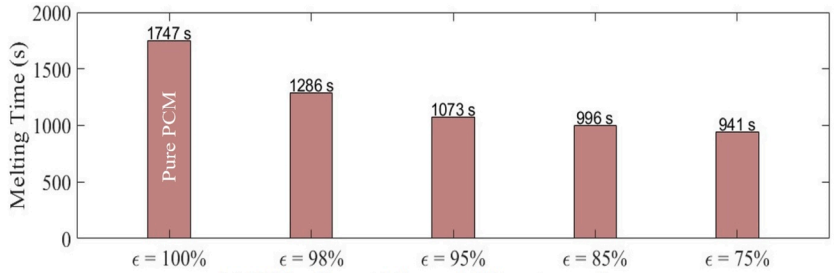


(a) PCM with metal foam of different porosity

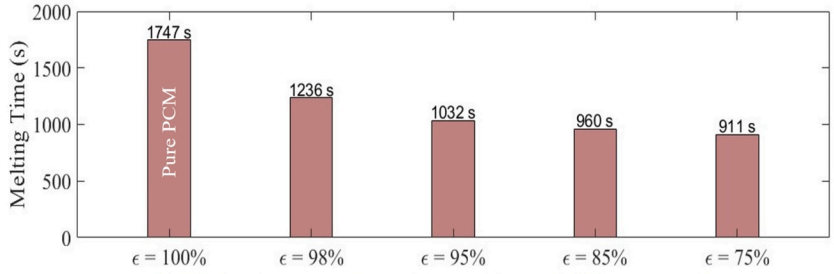


(b) 2% Graphene nanoPCM with metal foam of different porosity

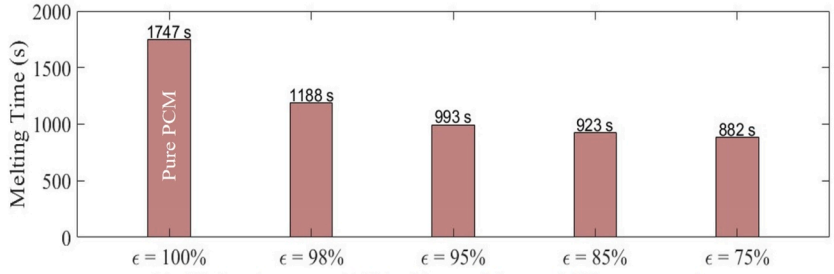


(c) 4% Graphene nanoPCM with metal foam of different porosity

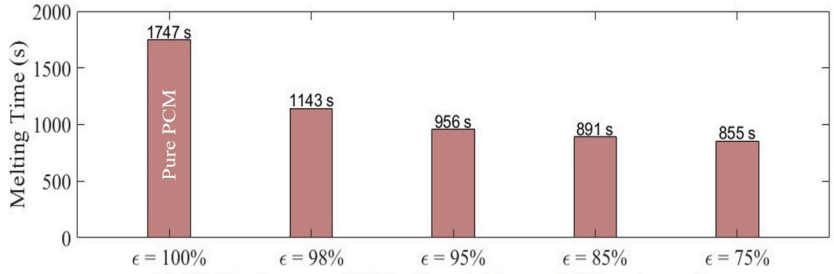


(d) 6% Graphene nanoPCM with metal foam of different porosity

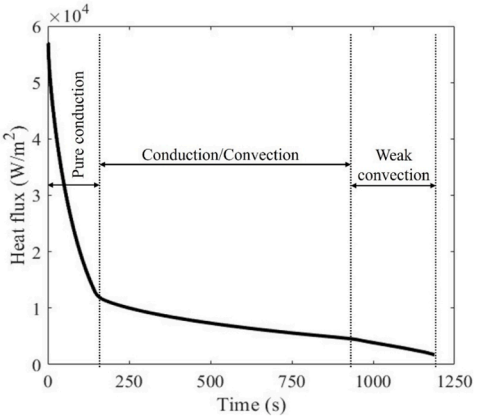


(e)

**Fig. 11.** Effect of (a) Metal foam porosity, (b – d) the combined use of metal foam and nanoparticles in PCM, (e) Change in heat flux during the melting/charging of PCM with both 6% graphene and metal foam of 98% porosity for T3F10 fin design configuration.

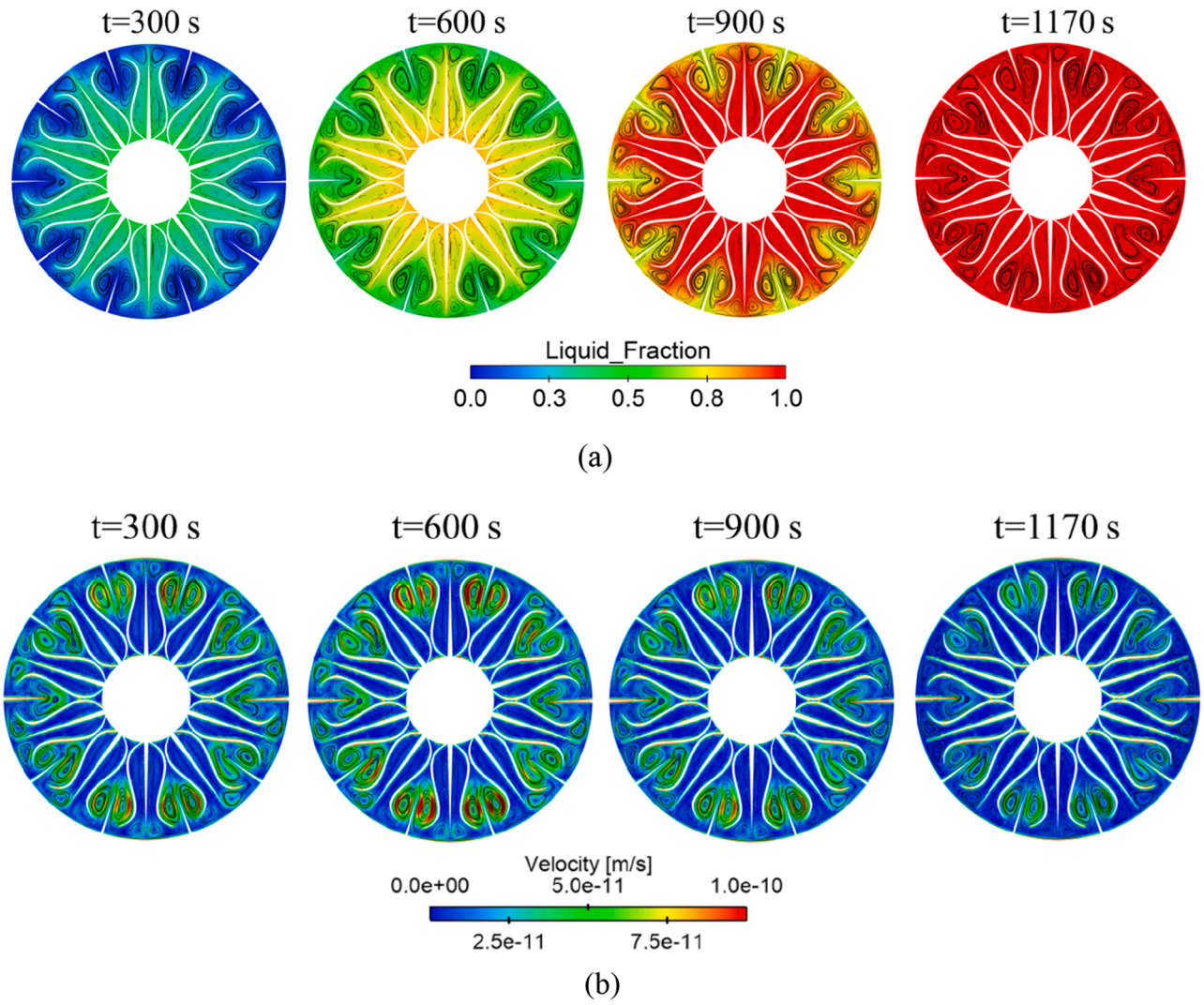


**Fig. 12.** (a) Liquid fraction contours of T3F10 fin design configuration with 6% graphene and copper foam with 98% porosity, and (b) Velocity contours with streamlines of T3F10 fin configuration with 6% graphene and copper foam with 98% porosity.

**Table 6**
Effect of nanoparticles and the porosity on charging/melting time saving in LHTES system.

| $\phi$ | Total duration required for complete melting of the PCM (in seconds) | | | | | Improvement in melting time (%) with nanoparticles or copper metal foam | | | | |
|---|---|---|---|---|---|---|---|---|---|---|
| | Non-porous | $\varepsilon$ | | | | Non-porous | $\varepsilon$ | | | |
| | | 0.98 | 0.95 | 0.85 | 0.75 | | 0.98 | 0.95 | 0.85 | 0.75 |
| 0.00 | 1747 | 1286 | 1073 | 996 | 941 | - | 26% | 39% | 43% | 46% |
| 0.02 | 1678 | 1236 | 1032 | 960 | 911 | 4% | 29% | 41% | 45% | 48% |
| 0.04 | 1647 | 1188 | 993 | 923 | 882 | 6% | 32% | 43% | 47% | 50% |
| 0.06 | 1614 | 1143 | 956 | 891 | 855 | 8% | 35% | 45% | 49% | 51% |

Fig. 14 illustrates the melting/charging durations of pure PCM for a LHTES system with a T3F10 fin design and other enhanced configurations. The T3F10 fin design configuration with pure PCM required approximately 1747 s to complete melting/charging. It serves as the reference as its performance is the best among all the other non-standard fin design configurations. The addition of 6 wt.% graphene reduced the melting/charging time to 1614 s, representing an 8% improvement. Introducing metal foam with 98% porosity resulted in a further reduction to 1286 s (26% improvement relative to the baseline case with having PCM only), attributed to the conductive network formed by the foam structure. When 6 wt.% graphene was combined with 98% porous metal foam, the melting/charging time decreased to 1143 s, achieving a 35% reduction. Reducing the foam porosity to 75% provided an even denser conductive pathway, yielding 941 s for PCM with metal foam alone (46% reduction) and 855 s for the combined graphene - metal foam system (51% reduction). This progressive decrease underscores the synergistic role of nanoparticle enhancement and metal foam integration, demonstrating their combined potential to accelerate phase transition and improve thermal energy storage efficiency.

To better quantify the relative contributions of natural convection, fin geometry, nanoparticles, and metal foam, the melting/charging times across different cases were compared. Natural convection alone reduced melting/charging time by ~12% compared to conduction-only (Fig. 5). Optimized lotus-inspired fins provided the largest effect, reducing melting/charging time by up to ~63% relative to sparse designs (T3S4, Fig. 7). Adding 6% graphene nanoparticles to the optimized

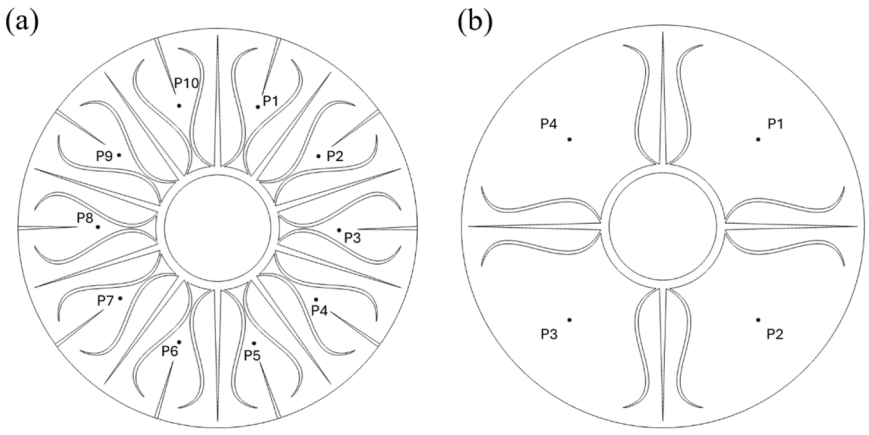


| T3F10 (Time = 600 s) | |
|---|---|
| Point | Liquid fraction |
| P1 | 0.2692 |
| P2 | 0.2582 |
| P3 | 0.2672 |
| P4 | 0.2811 |
| P5 | 0.2840 |
| P6 | 0.2866 |
| P7 | 0.2783 |
| P8 | 0.2853 |
| P9 | 0.2629 |
| P10 | 0.2674 |
| Mean | 0.2740 |
| **Std. Dev.** | **0.0095** |

| T3S4 (Time = 2280 s) | |
|---|---|
| Point | Liquid fraction |
| P1 | 0.2174 |
| P2 | 0.3976 |
| P3 | 0.3841 |
| P4 | 0.2173 |
| Mean | 0.3041 |
| **Std. Dev.** | **0.1000** |

**Fig. 13.** Standard deviation of liquid fraction in PCM for lotus-inspired (a) T3F10 fin configuration at t = 600 s and (b) T3S4 fin configuration at t = 2280 s.

fin case further reduced melting/charging time by ~7%, while CNT nanoparticles showed negligible or adverse effects at higher volume fractions (Fig. 9). Metal foams had a stronger impact, lowering melting/charging times by ~26% at 98% porosity and ~46% at 75% porosity relative to the fin-only case. The combined system (fins + 6% graphene + 75% porosity foam) achieved the shortest melting/charging time of 855 s, corresponding to a ~51% improvement compared to the fin-only baseline (1747 s). These results indicate that fin geometry is the dominant factor, foam provides major additional acceleration, and nanoparticles offer incremental gains. Natural convection, though modest alone, synergizes with fins and the metal foam to further enhance performance.

### 3.6. Cost analysis

$$\text{Melting/Charging Performance score} = \frac{1}{\textit{Melting/Charging time}^2\ \textit{price}^{0.5}\ \textit{volume}^{0.5}} \tag{40}$$

$$\text{Cost score} = \frac{1}{\textit{Melting/Charging time}^{0.5}\ \textit{price}^2\ \textit{volume}^{0.5}} \tag{41}$$

$$\text{Combined score} = \text{Melting/Charging Performance score} \times \text{Cost score} \tag{42}$$

Eqs. (40) – (42) are composite performance metrics proposed in this study to provide a balanced evaluation of different fin geometries by simultaneously accounting for thermal behavior, cost, and PCM volume. In Eq. (40), the melting/charging performance score penalizes longer melting/charging times (melting/charging time$^2$ term) while also incorporating the penalty of larger copper mass (through cost) and reduced PCM storage capacity (through volume). Conversely, Eq. (41), the cost score, emphasizes economic efficiency by penalizing expensive or copper-heavy designs more strongly (price$^2$ term) while giving a lower weight to melting/charging time and volume. The combined score in Eq. (42) integrates both aspects to identify designs that balance rapid thermal response with cost and volume considerations. Although these equations are not a standard convention in LHTES literature. This approach avoids bias toward any single factor and allows for a consistent comparison of geometries under different applications. These equations enable a fair comparison across diverse fin geometries and enhancement strategies (nanoparticles, foams, etc.), which otherwise differ widely in both thermal performance and cost implications. The non-dimensionalized form ensures that no single unit dominates; instead,

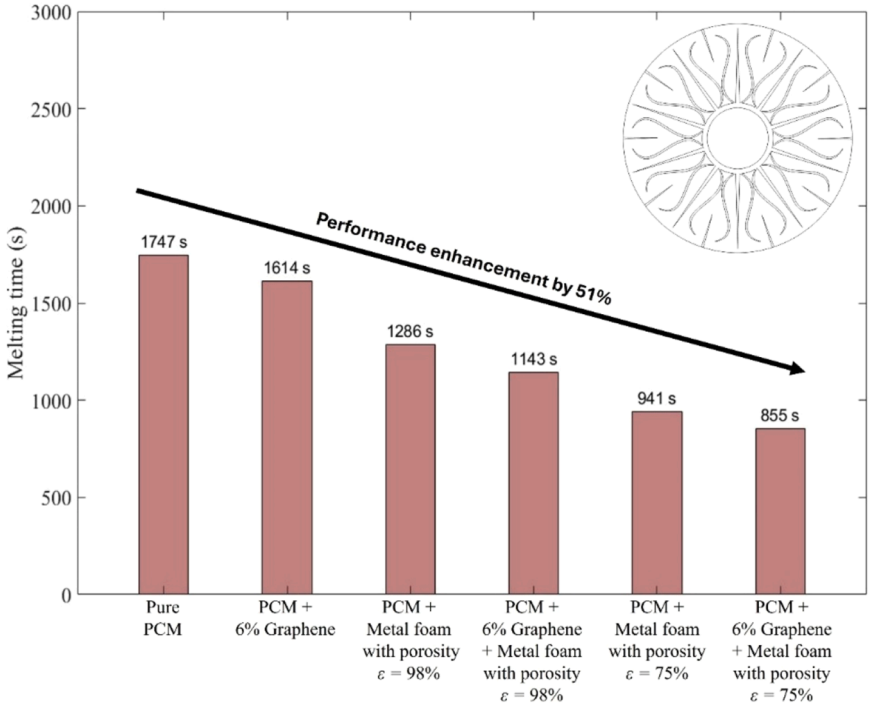


**Fig. 14.** The total melting time was evaluated for six cases for the T3F10 fin configuration: i) pure PCM, ii) PCM with 6% graphene, iii) PCM with a metal foam of 98% porosity, iv) PCM with both 6% graphene and metal foam with 98% porosity, v) PCM with a metal foam with 75% porosity, and vi) PCM with both 6% graphene and metal foam with 75% porosity.

the metrics express trade-offs in relative terms. The proposed performance, cost, and combined scores translate these competing objectives into non-dimensional indices, allowing systematic comparison across diverse configurations.

The correlation between fin perimeter and melting/charging time demonstrated a clear negative trend, with increased perimeter yielding shorter melting times. When all fifteen fin geometries were included, the regression model achieved an $R^2$ of 0.777, indicating that perimeter alone explained nearly 78% of the variation in melting/charging performance. However, five designs; T1NF, T2NF, T3NF, T3S4, and T3A4; exhibited anomalous behavior. The NF fin configuration lacks the central bridging rib observed in other designs, reducing conductive pathways, and resulting in melting/charging times between 2181 and 2618 seconds despite moderate or medium perimeters and can be considered outliers due to inherent design differences to the other 12 models. T3S4 and T3A4 combined very low perimeters (~0.548 m) with disproportionately high melting/charging times (4727 s and 4401 s, respectively). After excluding these outliers, the regression fit improved

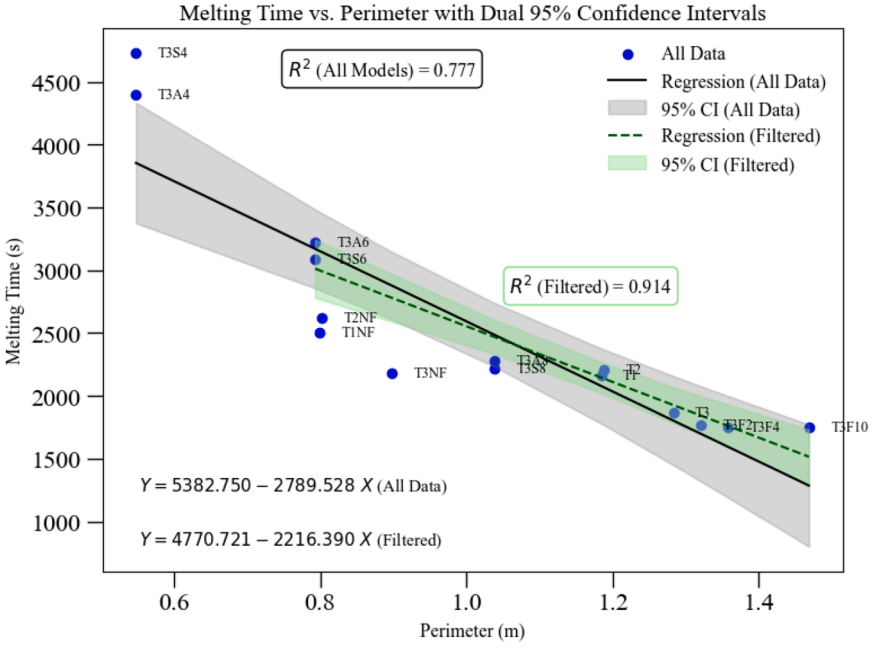


**Fig. 15.** Linear regression of melting time as a function of fin perimeter for all fifteen designs (black line) and the filtered dataset excluding NF variants (T1NF, T2NF, T3NF) and low-perimeter outliers (T3S4, T3A4) (dashed line). Shaded regions represent 95% confidence intervals for each fit.

**Table 7**
Ranked performance of fin designs based on cost, melting performance, and combined metrics. The melting performance score prioritizes rapid melting/charging, while the cost score emphasizes economic efficiency. The combined score identifies designs that balance melting/charging speed and cost.

| Model | Melting time (s) | Cost score | Rank by cost | Melting Performance score | Rank by Melting performance | Combined Score | Combined Ranking |
|---|---|---|---|---|---|---|---|
| T1 | 2159 | 3.8 | 6 | 12.3 | 5 | 46.2 | 7 |
| T2 | 2207 | 3.2 | 9 | 6.3 | 7 | 19.9 | 10 |
| T3 | 1864 | 4.2 | 5 | 19.2 | 4 | 80.6 | 6 |
| T3S6 | 3086 | 42.5 | 1 | 6.7 | 6 | 284.7 | 3 |
| T3S8 | 2218 | 5.7 | 3 | 6.2 | 8 | 35.1 | 8 |
| T3A6 | 3226 | 40.8 | 2 | 5.7 | 9 | 233.1 | 4 |
| T3A8 | 2276 | 5.3 | 4 | 4.9 | 10 | 26.2 | 9 |
| T3F2 | 1772 | 3.2 | 8 | 28.8 | 3 | 92.2 | 5 |
| T3F4 | 1747 | 3.8 | 7 | 107.1 | 1 | 402.6 | 1 |
| T3F10 | 1747 | 3.2 | 10 | 100.0 | 2 | 316.2 | 2 |

markedly to an $R^2$ of 0.914 (Fig. 15), confirming that perimeter is a strong and consistent predictor for the remaining geometries. The regression equations quantify this trend: for the full dataset, melting time (Y) in seconds is described by $Y = 5382.750 - 2789.528X$, and for the filtered dataset by $Y = 4770.721 - 2216.390X$, where X is the perimeter in meters. The filtered slope indicates that each additional meter of perimeter reduces melting/charging time by approximately 2216 s. This refinement also narrows the 95% confidence interval, evident in the lighter shaded band in Fig. 15, underscoring improved predictive accuracy for practical design ranges. Ranking of the designs (Table 7) was performed using three composite metrics: Melting/Charging Performance Score, Cost Score, and their product, the Combined Score. Each one is described by Eq. 40 - 42. The Melting/Charging Performance Score heavily penalizes long melting/charging times, while the Cost Score emphasizes low price. The Combined Score identifies designs that balance rapid melting/charging with cost efficiency. This dual framework avoids bias toward a single objective and provides flexibility for applications prioritizing either speed or economy.

High-perimeter fin designs T3F4 and T3F10 consistently ranked first and second in melting/charging performance, achieving melt times of 1747 s with perimeters exceeding 1.35 m. Their Combined Scores were also dominant, reflecting their ability to deliver fast response without extreme penalties in cost or volume. T3F2, with slightly lower perimeter (1.32 m) and a melt time of 1772 s, ranked third in Combined Score. In contrast, designs like T3S6 and T3A6, with perimeters near 0.79 m and melt/charge times around 3086 – 3226 s, performed modestly in Melting/Charging Performance but excelled in Cost Score due to significantly lower material volumes and prices. This contrast illustrates how cost-driven rankings favor moderate geometries that reduce copper mass without severely compromising melting/charging behavior. Split-fin variants such as T3S8 and T3A8 occupy mid-rank positions, offering balanced melting and cost characteristics but lacking the extremes of the F-series. The improved $R^2$ of 0.914 for filtered data demonstrates the robustness of perimeter as a predictive metric for early-stage fin optimization. Hence, perimeter alone provides a physically grounded and easily measurable design variable. Coupled with the multi-metric scoring framework, this approach facilitates rapid identification of designs tailored to application priorities, enabling either high-performance thermal response (T3F4/T3F10) or cost-sensitive storage solutions (T3S6/T3A6). Physically, the strong correlation between perimeter and melting/charging time reflects that a higher perimeter reduces the effective conduction distance within the PCM and promotes earlier onset of buoyancy-driven convection near fin surfaces. However, increasing the perimeter comes with some penalties, as it directly increases copper mass, cost, and reduces available PCM volume, thereby lowering energy density. Thus, perimeter serves as a robust early-stage optimization metric, but practical design requires balancing thermal gains against cost and storage capacity to identify geometries such as T3F4 (thermal priority) or T3S6 (cost priority).

The enhanced melting/charging rates demonstrated in this study have direct relevance for real-world systems where fast thermal response and compact storage are critical. In solar thermal collectors, a quicker PCM response reduces the mismatch between fluctuating solar input and storage uptake, thereby improving dispatchability and system reliability. In building applications, compact LHTES units can be integrated into HVAC and domestic hot water systems to shift peak loads, improve energy efficiency, and lower electricity costs during high-demand periods. In electronics cooling, rapid PCM charging/melting can prevent overheating during transient power spikes, extending device life and maintaining performance stability. In industrial waste heat recovery, hybrid fins and foams allow efficient capture and reuse of intermittent high-flux heat streams, improving overall process efficiency and reducing wasted energy.

## 4. Conclusion

This study presented a comprehensive numerical investigation of LHTES systems that integrate lotus-inspired fins, nanoparticles, hybrid nanoparticles, and copper metal foam to enhance charging/melting performance. The analysis examined the interplay of natural convection and conduction in paraffin wax (RT 82) under various fin configurations, nanoparticle concentrations, and foam porosities. The key findings are summarized as follows:

1. Natural convection reduced the total melting/charging time by ~12% compared to the conduction-only case. The effect was the strongest in the upper region of the PCM domain, while conduction dominated in the lower region, highlighting the need to balance both mechanisms through coordinated fin design strategies.
2. Among the 15 lotus-inspired fin design configurations analyzed in this study, higher fin density configurations (T3F10 and T3F4) along with natural convection, reduced melting/charging time by up to 63% compared to sparsely finned designs. The direct correlation of the fin perimeter with faster melting/charging established it as a key optimization parameter.
3. Graphene nano-PCM reduced melting/charging time by up to 6.9%, outperforming CNT-based nano-PCM due to higher conductivity. Hybrid mixtures of CNT and graphene did not yield additional benefits, and in some cases slowed melting/charging.
4. Copper foam accelerated melting/charging substantially, with the effect most pronounced at a lower porosity level of 75% due to dense conductive pathways. When combined with nanoparticles, the charging/melting time was reduced by more than 50%. An optimal balance was achieved with 6% graphene and 98% porosity foam, which maximize PCM's volume while maintaining a substantial improvement in the charging/melting rate.
5. The combination of lotus-inspired high perimeter fins, graphene nanoparticles, and copper foam achieved roughly a 51% reduction in melting/charging time, while also improving storage density and ensuring uniform phase-change behavior.

6. High-perimeter fins (T3F4, T3F10) achieved the fastest melting/charging (~1747 s) but at a higher material cost. Moderate perimeter designs (T3S6, T3A6) reduced material use by 40 –45% and achieved melting/charging times of ~3086 – 3226 s, making them a cost-effective alternative for cost-sensitive applications.

Overall, the results demonstrate that nature-inspired lotus-shaped fin designs, particularly when combined with graphene nanoparticles and copper foam, can effectively enhance the compactness, thermal response, and operational efficiency of LHTES systems. Such improvements are directly relevant to solar thermal technologies, building thermal management, and industrial waste-heat recovery, where faster charging/melting and higher energy density improve overall system performance and reduce costs.

## 5. Drawbacks

The present simulations and results are subject to several assumptions. Thermophysical properties of PCMs/nano-PCMs were assumed constant (except density), natural convection was modeled as laminar, and viscous dissipation, volume shrinkage during phase change, and radiative heat transfer were neglected. Nanoparticles were considered to be uniformly dispersed without agglomeration, and the metallic foams were treated as homogeneous isotropic porous structures. Furthermore, a two-dimensional model was employed to reduce computational cost and capture dominant radial melting/charging behavior; however, this approach cannot fully represent three-dimensional effects such as complex convective flow structures and vortex formation. These aspects represent limitations of the current study and highlight important directions for future work, including extension to fully 3D simulations and experimental validation, beyond model-to-model validations. In addition, while the present work emphasizes thermal performance, future studies will need to evaluate pressure-drop impacts, manufacturing feasibility, and life-cycle costs to establish the full techno-economic potential of lotus-inspired fin designs.

## 6. Future work

To build on the present study, future research will extend the model to three-dimensional simulations to capture more detailed natural convection effects and complex flow structures that cannot be fully represented in two dimensions. Experimental validation of lotus-shaped fin configurations will also be undertaken to corroborate the numerical predictions and assess practical manufacturability. In addition, future studies will incorporate exergy efficiency and thermal effectiveness analyses to evaluate not only the melting/charging rate but also the overall thermodynamic performance of the system. This broader perspective will provide a more comprehensive assessment of how geometric and material modifications influence both the speed and efficiency of latent heat thermal energy storage.

## CRediT authorship contribution statement

**Prashant Saini:** Writing – original draft, Visualization, Validation, Formal analysis, Conceptualization. **Julian D. Osorio:** Writing – review & editing, Supervision, Conceptualization. **Munjal P. Shah:** Writing – review & editing, Visualization, Formal analysis, Conceptualization. **Umang N. Patel:** Writing – review & editing, Visualization, Formal analysis, Conceptualization. **Akhil Nelapudi:** Writing – review & editing, Formal analysis. **Luis A. Porto-Hernandez:** Writing – review & editing, Formal analysis.

## Declaration of competing interest

The authors declare that they have no known competing financial interests or personal relationships that could have appeared to influence the work reported in this paper.

## Acknowledgments

This work was authored by the National Renewable Energy Laboratory, operated by Alliance for Sustainable Energy, LLC, for the U.S. Department of Energy (DOE) under Contract No. DE-AC36-08GO28308. Funding provided by the U.S. Department of Energy Office (DOE) - Water Power Technologies Office (WPTO) – Project Agreement 2.2.5.402 - Harnessing Ocean thermal gradients using thermoelectric-based submersibles for ocean power applications. The views expressed in the article do not necessarily represent the views of the DOE or the U. S. Government. The U.S. Government retains and the publisher, by accepting the article for publication, acknowledges that the U.S. Government retains a nonexclusive, paid-up, irrevocable, worldwide license to publish or reproduce the published form of this work, or allow others to do so, for U.S. Government purposes.

## Data availability

Data will be made available on request.

## References

[1] K.M. Kennedy, T.H. Ruggles, K. Rinaldi, J.A. Dowling, L. Duan, K. Caldeira, et al., The role of concentrated solar power with thermal energy storage in least-cost highly reliable electricity systems fully powered by variable renewable energy, Adv. Appl. Energy 6 (2022) 100091.
[2] H. Zhang, J. Baeyens, G. Cáceres, J. Degrève, Y. Lv, Thermal energy storage: recent developments and practical aspects, Prog. Energy Combust. Sci. 53 (2016) 1–40.
[3] Saini P, Patil DV, Powar S. Review on integration of solar air heaters with thermal energy storage. In: Tyagi H, Agarwal AK, Chakraborty PR, Powar S, *Applications of Solar Energy*. Singapore: Springer; 2018 [cited 2024 Sep 9]. p. 163-86. Available from: https://doi.org/10.1007/978-981-10-7206-2_9.
[4] Z. Yin, J. Zheng, H. Kim, Y. Seo, P. Linga, Hydrates for cold energy storage and transport: a review, Adv. Appl. Energy 2 (2021) 100022.
[5] Y.B. Tao, YL. He, A review of phase change material and performance enhancement method for latent heat storage system, Renew. Sustain. Energy Rev. 93 (2018) 245–259.
[6] A.J. Carrillo, J. González-Aguilar, M. Romero, JM. Coronado, Solar energy on demand: a review on high-temperature thermochemical heat storage systems and materials, Chem. Rev. 119 (7) (2019) 4777–4816.
[7] T. Bauer, N. Pfleger, N. Breidenbach, M. Eck, D. Laing, S. Kaesche, Material aspects of solar salt for sensible heat storage, Appl. Energy 111 (2013) 1114–1119.
[8] X. Huang, S. Yao, X. Yang, R. Zhou, Melting performance assessments on a triplex-tube thermal energy storage system: optimization based on response surface method with natural convection, Renew. Energy 188 (2022) 890–910.
[9] B. Cárdenas, N. León, High temperature latent heat thermal energy storage: phase change materials, design considerations and performance enhancement techniques, Renew. Sustain. Energy Rev. 27 (2013) 724–737.
[10] W. Aftab, A. Usman, J. Shi, K. Yuan, M. Qin, R. Zou, Phase change material-integrated latent heat storage systems for sustainable energy solutions, Energy Environ. Sci. 14 (8) (2021) 4268–4291.
[11] X. Huang, S. Yao, X. Yang, R. Zhou, J. Luo, X. Shen, Comparison of solidification performance enhancement strategies for a triplex-tube thermal energy storage system, Appl. Therm. Eng. 204 (2022) 117997.
[12] N. Hu, Z.R. Li, Z.W. Xu, LW. Fan, Rapid charging for latent heat thermal energy storage: a state-of-the-art review of close-contact melting, Renew. Sustain. Energy Rev. 155 (2022) 111918.
[13] P. Saini, JD. Osorio, Review on phase change materials and thermoelectric generators for ocean thermal gradient applications, Renew. Sustain. Energy Rev. 219 (2025) 115851.
[14] Q. Li, C. Li, Z. Du, F. Jiang, Y. Ding, A review of performance investigation and enhancement of shell and tube thermal energy storage device containing molten salt-based phase change materials for medium and high temperature applications, Appl. Energy 255 (2019) 113806.
[15] P. Saini, A. Dhar, S. Powar, M. Doddamani, Cesaro fins parametric optimization for enhancement in the solidification performance of a latent heat storage system with combined fins, foam, and nanoparticle, Energy Rep. 9 (2023) 5670–5687.
[16] P. Saini, A. Dhar, S. Powar, Parametric optimization of a cesaro fins employed latent heat storage system for melting performance enhancement, J. Energy Storage 51 (2022) 104534.
[17] M. Alizadeh, Hosseinzadeh Kh, M.H. Shahavi, DD. Ganji, Solidification acceleration in a triplex-tube latent heat thermal energy storage system using V-shaped fin and nano-enhanced phase change material, Appl. Therm. Eng. 163 (2019) 114436.
[18] A. Sciacovelli, F. Gagliardi, V. Verda, Maximization of performance of a PCM latent heat storage system with innovative fins, Appl. Energy 137 (2015) 707–715.

[19] G. Humbert, Y. Ding, A. Sciacovelli, Combined enhancement of thermal and chemical performance of closed thermochemical energy storage system by optimized tree-like heat exchanger structures, Appl. Energy 311 (2022) 118633.
[20] Hosseinzadeh Kh, M. Alizadeh, M.H. Alipour, B. Jafari, DD. Ganji, Effect of nanoparticle shape factor and snowflake crystal structure on discharging acceleration LHTESS containing (Al2O3-GO) HNEPCM, J. Mol. Liq. 289 (2019) 111140.
[21] L. Wu, X. Zhang, X. Liu, Numerical analysis and improvement of the thermal performance in a latent heat thermal energy storage device with spiderweb-like fins, J. Energy Storage 32 (2020) 101768.
[22] Y. Huang, Q. Han, X. Liu, Experimental investigation on the melting and solidification performance enhancement of a fractal latent heat storage unit, Int. J. Heat. Mass Transf. 179 (2021) 121640.
[23] Y. Huang, X. Liu, Charging and discharging enhancement of a vertical latent heat storage unit by fractal tree-shaped fins, Renew. Energy 174 (2021) 199–217.
[24] J.D. Osorio, A. Rivera-Alvarez, JC. Ordonez, Shape optimization of thin flat plate fins with geometries defined by linear piecewise functions, Appl. Therm. Eng. 112 (2017) 572–584.
[25] L. Pu, S. Zhang, L. Xu, Y. Li, Thermal performance optimization and evaluation of a radial finned shell-and-tube latent heat thermal energy storage unit, Appl. Therm. Eng. 166 (2020) 114753.
[26] Y. Zhang, B. Lu, Z. Wang, J. Zhu, J. Zhang, C. Wang, Experimental investigation on the charging and discharging performance enhancement of a vertical latent heat thermal energy storage unit via snowflake fin design, Int. J. Heat. Mass Transf. 199 (2022) 123455.
[27] A. Rozenfeld, Y. Kozak, T. Rozenfeld, G. Ziskind, Experimental demonstration, modeling and analysis of a novel latent-heat thermal energy storage unit with a helical fin, Int. J. Heat. Mass Transf. 110 (2017) 692–709.
[28] Q. Mao, Y. Zhu, T. Li, Study on heat storage performance of a novel bifurcated finned shell-tube heat storage tank, Energy 263 (2023) 125636.
[29] Z. Elmaazouzi, I.A. Laasri, A. Gounni, M.E. Alami, EG. Bennouna, Enhanced thermal performance of finned latent heat thermal energy storage system: fin parameters optimization, J. Energy Storage 43 (2021) 103116.
[30] C. Nie, S. Deng, J. Liu, Effects of fins arrangement and parameters on the consecutive melting and solidification of PCM in a latent heat storage unit, J. Energy Storage 29 (2020) 101319.
[31] S.A. Zonouzi, A. Dadvar, Numerical investigation of using helical fins for the enhancement of the charging process of a latent heat thermal energy storage system, J. Energy Storage 49 (2022) 104157.
[32] F. He, R. Bo, C. Hu, X. Meng, W. Gao, Employing spiral fins to improve the thermal performance of phase-change materials in shell-tube latent heat storage units, Renew. Energy 203 (2023) 518–528.
[33] S. Zhang, L. Pu, L. Xu, R. Liu, Y. Li, Melting performance analysis of phase change materials in different finned thermal energy storage, Appl. Therm. Eng. 176 (2020) 115425.
[34] M.J. Zarei, H. Bazai, M. Sharifpur, O. Mahian, B. Shabani, The effects of fin parameters on the solidification of PCMs in a fin-enhanced thermal energy storage system, Energies 13 (1) (2020) 198.
[35] M.E. Nakhchi, JA. Esfahani, Improving the melting performance of PCM thermal energy storage with novel stepped fins, J. Energy Storage 30 (2020) 101424.
[36] X. Yang, J. Guo, B. Yang, H. Cheng, P. Wei, YL. He, Design of non-uniformly distributed annular fins for a shell-and-tube thermal energy storage unit, Appl. Energy 279 (2020) 115772.
[37] H. Wang, H. Xu, C. Liu, Z. Zhang, X. Ling, F. Jiang, Numerical investigation of melting enhancement for paraffin in an innovative finned-plate latent heat thermal energy storage unit, J. Energy Storage 43 (2021) 103222.
[38] R. Baby, C. Balaji, Thermal optimization of PCM-based pin fin heat sinks: an experimental study, Appl. Therm. Eng. 54 (1) (2013) 65–77.
[39] J.M. Mahdi, EC. Nsofor, Solidification enhancement of PCM in a triplex-tube thermal energy storage system with nanoparticles and fins, Appl. Energy 211 (2018) 975–986.
[40] S. Wu, H. Wang, S. Xiao, D. Zhu, Numerical simulation on thermal energy storage behavior of Cu/paraffin nanofluids PCMs, Procedia Eng. 31 (2012) 240–244.
[41] Hosseinzadeh Kh, M.A.E. Moghaddam, A. Asadi, A.R. Mogharrebi, DD. Ganji, Effect of internal fins along with hybrid nanoparticles on solid process in star shape triplex latent heat thermal energy storage system by numerical simulation, Renew. Energy 154 (2020) 497–507.
[42] J.M. Khodadadi, SF. Hosseinizadeh, Nanoparticle-enhanced phase change materials (NEPCM) with great potential for improved thermal energy storage, Int. Commun. Heat. Mass Transf. 34 (5) (2007) 534–543.
[43] J.M. Mahdi, EC. Nsofor, Melting enhancement in triplex-tube latent heat energy storage system using nanoparticles–metal foam combination, Appl. Energy 191 (2017) 22–34.
[44] J.M. Mahdi, EC. Nsofor, Melting enhancement in triplex-tube latent thermal energy storage system using nanoparticles–fins combination, Int. J. Heat. Mass Transf. 109 (2017) 417–427.
[45] AA. Mohamad, Myth about nano-fluid heat transfer enhancement, Int. J. Heat. Mass Transf. 86 (2015) 397–403.
[46] A. Hosseinpour, M. Pourfallah, M. Gholinia, Improving energy storage by PCM using hybrid nanofluid [(SWCNTs-CuO)/H2O] and a helical (spiral) coil: hybrid passive techniques, Theor. Appl. Mech. Lett. 13 (4) (2023) 100458.
[47] E.A. Hassan, M.A. Tony, MM. Awad, Thermal energy storage using hybrid nanofluid phase change material based on waste sludge incorporating ZnO/α-Fe2O3, Nanomaterials 14 (7) (2024) 604.
[48] Aljabair S, Sadiq IE. Effect of Al2O3/CuO Hybrid Nanoparticles Dispersion on Melting Process of PCM in a Triplex Tube Heat Storage. Rochester (NY): Social Science Research Network; 2025 [cited 2025 Aug 31]. Available from: https://papers.ssrn.com/sol3/papers.cfm?abstract_id=4463287.
[49] C.Y. Zhao, W. Lu, Y. Tian, Heat transfer enhancement for thermal energy storage using metal foams embedded within phase change materials (PCMs), Sol. Energy 84 (8) (2010) 1402–1412.
[50] Z. Chen, D. Gao, J. Shi, Experimental and numerical study on melting of phase change materials in metal foams at pore scale, Int. J. Heat. Mass Transf. 72 (2014) 646–655.
[51] W.Q. Li, Z.G. Qu, Y.L. He, WQ. Tao, Experimental and numerical studies on melting phase change heat transfer in open-cell metallic foams filled with paraffin, Appl. Therm. Eng. 37 (2012) 1–9.
[52] D. Zhou, CY. Zhao, Experimental investigations on heat transfer in phase change materials (PCMs) embedded in porous materials, Appl. Therm. Eng. 31 (5) (2011) 970–977.
[53] X. Yang, Z. Guo, Y. Liu, L. Jin, Y.L. He, Effect of inclination on the thermal response of composite phase change materials for thermal energy storage, Appl. Energy 238 (2019) 22–33.
[54] W.B. Ye, M. Arıcı, Redefined interface error, 2D verification and validation for pure solid-gallium phase change modeling by enthalpy-porosity methodology, Int. Commun. Heat. Mass Transf. 147 (2023) 106952.
[55] W.B. Ye, M. Arıcı, 3D validation, 2D feasibility, corrected and developed correlations for pure solid-gallium phase change modeling by enthalpy-porosity methodology, Int. Commun. Heat. Mass Transf. 144 (2023) 106780.
[56] W.B. Ye, M. Arıcı, Exploring mushy zone constant in enthalpy-porosity methodology for accurate modeling convection-diffusion solid-liquid phase change of calcium chloride hexahydrate, Int. Commun. Heat. Mass Transf. 152 (2024) 107294.
[57] W.B. Ye, M. Arıcı, False diffusion, asymmetrical interface, and equilibrious state for pure solid-gallium phase change modeling by enthalpy-porosity methodology, Int. Commun. Heat. Mass Transf. 144 (2023) 106746.
[58] K. Teather, K. Siddiqui, An experimental investigation of constrained melting of a phase change material in circular geometries. Part II: temperature characterization, J. Energy Storage 86 (2024) 110206.
[59] L. Lin, D. Yang, Z. Luo, D. Liu, S.P. Lohani, S. Jia, et al., Numerical study on melting and heat transfer characteristics of vertical cylindrical PCM with a focus on the solid–liquid interface heat transfer rate, J. Energy Storage 72 (2023) 108370.
[60] S. Liu, H. Peng, Z. Hu, X. Ling, J. Huang, Solidification performance of a latent heat storage unit with innovative longitudinal triangular fins, Int. J. Heat. Mass Transf. 138 (2019) 667–676.
[61] M. Kazemi, M.J. Hosseini, A.A. Ranjbar, R. Bahrampoury, Improvement of longitudinal fins configuration in latent heat storage systems, Renew. Energy 116 (2018) 447–457.
[62] ANSYS Inc, Fluent User's Guide, ANSYS Inc., Canonsburg (PA), 2025.
[63] Kherbeet ASh, H.A. Mohammed, BH. Salman, The effect of nanofluids flow on mixed convection heat transfer over microscale backward-facing step, Int. J. Heat. Mass Transf. 55 (21) (2012) 5870–5881.
[64] Hosseinzadeh Kh, A. Asadi, A.R. Mogharrebi, M.E. Azari, DD. Ganji, Investigation of mixture fluid suspended by hybrid nanoparticles over vertical cylinder by considering shape factor effect, J. Therm. Anal. Calorim. 143 (2) (2021) 1081–1095.
[65] V.V. Calmidi, RL. Mahajan, Forced convection in high porosity metal foams, J. Heat. Transf. 122 (3) (2000) 557–565.
[66] A. Žukauskas, Heat transfer from tubes in crossflow, in: J.P. Hartnett, T.F. Irvine (Eds.), Advances in Heat Transfer, Academic Press, New York, 1972, pp. 93–160 [cited 2025 Jun 20].Available from: https://www.sciencedirect.com/science/article/pii/S0065271708700388.
[67] A.A. Al-Abidi, S. Mat, K. Sopian, M.Y. Sulaiman, M. AbdulrahmanTh, Experimental study of melting and solidification of PCM in a triplex tube heat exchanger with fins, Energy Build. 68 (2014) 33–41.
[68] B. Palmer, A. Arshad, Y. Yang, C. Wen, Energy storage performance improvement of phase change materials-based triplex-tube heat exchanger using liquid–solid interface-informed fin configurations, Appl. Energy 333 (2023) 120576.
[69] V.R. Voller, C. Prakash, A fixed grid numerical modelling methodology for convection–diffusion mushy region phase-change problems, Int. J. Heat. Mass Transf. 30 (8) (1987) 1709–1719.
[70] A. Ebrahimi, C.R. Kleijn, IM. Richardson, Sensitivity of numerical predictions to the permeability coefficient in simulations of melting and solidification using the enthalpy-porosity method, Energies 12 (22) (2019) 4360.
[71] A.D. Brent, V.R. Voller, KJ. Reid, Enthalpy-porosity technique for modeling convection–diffusion phase change: application to the melting of a pure metal, Numer. Heat. Transf. 13 (3) (1988) 297–318.
[72] A.A. Al-Abidi, S. Mat, K. Sopian, M.Y. Sulaiman, Mohammad ATh, Internal and external fin heat transfer enhancement technique for latent heat thermal energy storage in triplex tube heat exchangers, Appl. Therm. Eng. 53 (1) (2013) 147–156.
[73] T. Abdulrazzaq, H. Togun, J.M. Mahdi, H.I. Mohammed, F.L. Rashid, A.F. Khalaf, et al., Evaluation of multi-branch fin inserts for improved thermal response in latent

heat storage systems: a numerical approach, Case Stud. Therm. Eng. 73 (2025) 106464.
[74] A.M. Ali, A. Bagdanavicius, E.R. Barbour, D.L. Pottie, S. Garvey, J. Rouse, et al., Improving the performance of a shell and tube latent heat thermal energy storage through modifications of heat transfer pipes: a comprehensive investigation on various configurations, J. Energy Storage 96 (2024) 112678.
[75] A. Shahraki, A. Tavakoli, M. Mohammadi, A. Ebrahimi, A. Kianifar, Enhancing the charging performance of a triplex-tube thermal energy storage system using fins and nanoparticles, Therm. Sci. Eng. Prog. 62 (2025) 103565.
[76] A. Tavakoli, J. Hashemi, M. Najafian, A. Ebrahimi, Physics-based modelling and data-driven optimisation of a latent heat thermal energy storage system with corrugated fins, Renew. Energy 217 (2023) 119200.
[77] R.S. Vajjha, DK. Das, Experimental determination of thermal conductivity of three nanofluids and development of new correlations, Int. J. Heat. Mass Transf. 52 (21) (2009) 4675–4682.